

Intra-mitochondrial disulfide polymerization controls cancer cell necroptosis

Sangpil Kim

Ulsan National Institute of Science and Technology

Batakrishna Jana

Ulsan National Institute of Science and Technology

Eun Min Go

Ulsan National Institute of Science and Technology

Ji Eun Lee

Ulsan National Institute of Science and Technology

Seongeon Jin

Ulsan National Institute of Science and Technology

Youjung Sim

Ulsan National Institute of Science and Technology

Sehee Son

Ulsan National Institute of Science and Technology

Dohyun Kim

Ulsan National Institute of Science and Technology

Chaekyu Kim

Ulsan National Institute of Science and Technology <https://orcid.org/0000-0002-3269-6095>

Sang Kyu Kwak

Ulsan National Institute of Science and Technology <https://orcid.org/0000-0002-0332-1534>

Ja-Hyoung Ryu (✉ jhryu@unist.ac.kr)

Ulsan National Institute of Science and Technology <https://orcid.org/0000-0003-0252-0985>

Article

Keywords: in-situ polymerization, polymer science, anticancer treatment

Posted Date: February 12th, 2021

DOI: <https://doi.org/10.21203/rs.3.rs-86561/v1>

License:   This work is licensed under a Creative Commons Attribution 4.0 International License.

[Read Full License](#)

Intra-mitochondrial disulfide polymerization controls cancer cell necroptosis

Sangpil Kim^{1,†}, Batakrisna Jana^{1,†}, Eun Min Go^{2,†}, Ji Eun Lee², Seongeon Jin¹, Youjung Sim¹, Sehee Son¹, Dohyun Kim¹, Chaekyu Kim,¹ Sang Kyu Kwak^{*2}, Ja-Hyoung Ryu^{*1}

¹Department of Chemistry, Ulsan National Institute of Science and Technology (UNIST), Ulsan 44919, Republic of Korea. Republic of Korea.

²Department of Energy Engineering, School of Energy and Chemical Engineering, Ulsan National Institute of Science and Technology (UNIST), Ulsan 44919, Republic of Korea

Correspondence: E-mail: jhryu@unist.ac.kr; skkwak@unist.ac.kr

Abstract

In a biological system, energy-consuming reactions to attain a biological dissipative state are ubiquitous, and mimicking such reactions is a great challenge in synthetic chemistry. Herein, we report an intra-mitochondrial polymerization strategy for constructing macroscopic structures using a reactive oxygen species (ROS)-dissipative system. This is the first time that the occurrence of disulfide polymerization inside cancer mitochondria owing to the high ROS concentration of cancer mitochondria is reported. This polymerization hardly occurred inside cells owing to the intracellular reductive environment. The polymerization process of a thiol-containing monomer further increases the ROS level inside the mitochondria, thereby enabling the autocatalytic process to accelerate polymerization and induce mitochondrial dysfunction. This *in-situ* polymerization shows great potential for anticancer treatment against various cancer cell lines, including drug-resistant cancer cells.

Intracellular biomacromolecules, such as proteins, DNA, and polysaccharides, are synthesized by polymerization of small molecules, including amino acids and nucleotides. Unlike small molecules, biomacromolecules show distinct properties and play important roles in cellular processes.¹⁻⁵ For instance, amino acids themselves display no enzymatic activities and exhibit trivial interactions with proteins. In contrast, proteins formed by the self-assembly of several polypeptides into well-ordered 3D or 4D structures often show enzymatic activities. Proteins also play key roles in vital cellular signaling pathways involving protein-protein interactions.^{6,7} Notably, the functions of these biomolecules strongly depend on their structures; therefore, disruptions of the protein assemblies significantly affect their properties, often leading to deactivation.⁶ Research in the field of supramolecular chemistry has demonstrated the possibility of creating artificial intracellular assembly systems, which could imitate the biological and pharmaceutical functionalities of proteins.⁸⁻¹² It has been shown that small peptide-based amphiphilic molecules formed ordered structures inside cells. It is noteworthy that such systems exhibited intriguing interactions with biomacromolecules, enabling delivery of cargo into intracellular organelles, sequestering intracellular enzymes, and selectively causing cancer cell death.¹³⁻¹⁹ Nevertheless, the formation of such ordered structures is dependent on the self-assembly equilibrium and requires high concentrations of small molecules, which is a result of a large entropic penalty associated with assembling ordered structures. Thus, this approach has significant limitations, including dynamic instability.²⁰

Polymerization-induced self-assembly (PISA) takes advantage of the chain-end reactivity of solvophilic macromolecules for the polymerization of a second monomer. Importantly, the growth of the second block, which is insoluble in the medium, results in the formation of block copolymers that self-assemble into nanoparticles via an entropy-driven chain collapse.^{21,22} PISA has been demonstrated as a promising technique for the synthesis of polymeric materials used in drug delivery, medical imaging, and tissue culture.^{23,24} It has been speculated that conducting PISA in living cells to construct artificial biological systems would enable intracellular formation of synthetic nanostructures with the ability to effectively interact with biomolecules. This would offer an opportunity to control cellular function, providing inspiration for the design of novel therapeutics. Several recent reports have described the potential of this approach. For example, *in situ* biosyntheses of inorganic nanomaterials by intracellular polymerization^{25,26} and intracellular radical polymerization were successfully achieved.^{27,28} Nevertheless, intracellular PISA leading to modification of the cellular fate

remains a challenge. In this study, we report intramitochondrial polymerization to construct an artificial structure able to regulate cellular function for the first time.

Herein, a disulfide bond was used as a polymerizable functional group. Disulfide bonds are dynamic covalent bonds, which are in equilibrium between a disulfide and two thiols. This allowed for the construction of a dynamic combinatorial library of macrocycles, some of which formed fiber structures through autocatalytic reactions.²⁹⁻³¹ However, dissipative out-of-equilibrium state is common in nature. Consequently, instead of the formation of disulfide bonds, the presence of large amounts of a reducing agent (e.g., glutathione [GSH]) results in their destruction. Interestingly, in this study, we found that another type of dissipative reaction, namely disulfide polymerization, took place inside the mitochondria (**Fig 1**). The monomer was synthesized by conjugation of an aromatic molecule containing two thiol groups with a mitochondria-targeting unit, i.e., triphenylphosphonium (TPP). The resulting mitochondria-targeting monomers accumulated in the mitochondria of cancer cells, because compared with normal cells, the membranes of these organelles in cancer cells are more negatively charged.³²⁻³⁴ It is known that ROS are overproduced in the mitochondria of cancer cells; therefore, they could be utilized as chemical fuel. Oxidative agents catalyze the oxidation of thiol groups to form disulfide polymers.^{35,36} Furthermore, it has also been shown that the polymerization process induces oxidative stress in the mitochondria, leading to increased levels of ROS, which act as autocatalytic agents to catalyze further polymerization. Finally, the polymerization process induces self-assembly of the molecules into fibrous structures, resulting in mitochondrial dysfunction and activation of necroptosis.

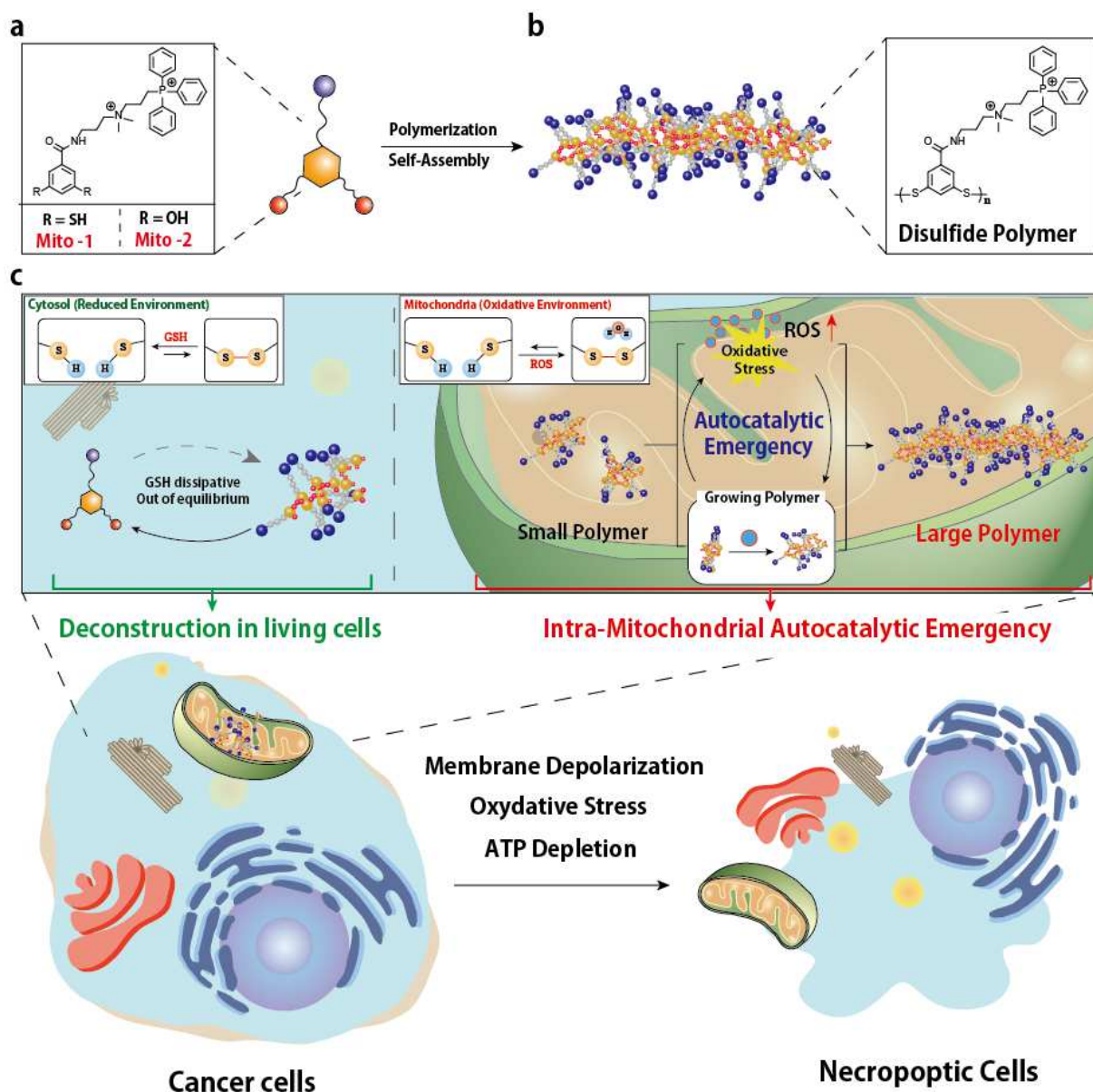


Fig. 1 | Intramitochondrial polymerization-induced self-assembly (Mito-PISA). Schematic illustration of Mito-PISA for controlling cancer cell necroptosis. **a**, Chemical structure of the monomer and **b**, polymerization-induced assembly by a disulfide polymer. **c**, Intramitochondrial polymerization can induce necroptosis and lead to mitochondrial dysfunction in cancer cells. Generally, the formation of disulfide bonds is prohibited by the intracellular reductive environment. However, intramitochondrial accumulation of monomers facilitates polymerization, resulting in oxidative stress and generation of ROS. Increased levels of ROS provide effective conditions for the formation of large polymers, leading to mitochondrial dysfunction and activation of the necroptosis signaling pathway.

Results and discussion

PISA using a disulfide bond. The target monomer (**Mito-1**) for intracellular polymerization was synthesized by the conjugation of an aromatic dithiol with a quaternary ammonium-modified triphenylphosphonium (TPP) species via 1-ethyl-3-(3-dimethylaminopropyl)carbodiimide (EDC) coupling. The resulting product was purified by high-performance liquid chromatography (HPLC). To confirm the functionality of the polymerization, a control molecule (**Mito-2**) containing dihydroxy moieties instead of dithiol groups (**Fig. 1**) was also prepared. The polymerization of **Mito-1** in phosphate-buffered saline (PBS) at pH 8 was first analyzed by HPLC and gel permeation chromatography (GPC). As demonstrated in **Fig. 2a**, the intensity of the peak corresponding to **Mito-1** (10 mM) sharply decreased within 4 h. It was determined that after 4 h, 80% of the monomer was consumed and the molecular weight of resulting polymer was established at 1.8×10^4 g/mol. In addition, the polydispersity index (PDI) was calculated at 2.3. Conversely, the intensity of the peak attributed to **Mito-2** and the molecular weight of the monomer remained unchanged (**Fig. 2a**). This indicated that the thiol groups in **Mito-1** were oxidized to form disulfide bonds, generating a polymer.

In general, disulfide bonds easily decompose under reducing conditions, such as the cellular environment.^{37,38} Thus, the occurrence of disulfide polymerization inside living cells is remarkably rare. Nonetheless, we speculated that if the concentration of the dithiol monomer was sufficiently high, disulfide polymerization could take place. Hence, the concentration-dependent polymerization of **Mito-1** was investigated in PBS (pH 8) in the presence of 10 mM GSH to mimic the intramitochondrial environment. The intensity of the peak corresponding to the monomer was monitored at various concentrations of the compound (1 and 10 mM). When 10 mM of the monomer was used, the intensity of the peak considerably decreased after 6 h. In contrast, no significant decrease was observed at 1 mM (**Fig. 2b**). This suggested that polymerization did not occur at low concentrations of the monomer due to high levels of GSH (10 mM), which resulted in the reduction of disulfide bonds. However, high concentrations of the monomer shifted the equilibrium of the dynamic covalent bond toward the bond formation reaction rather than decomposition, thus enabling the occurrence of polymerization in a reducing environment.

Intriguingly, we found that the self-assembling behavior depended on the concentration of the monomer during polymerization. Dynamic light scattering (DLS) analysis revealed that

both 1 mM and 10 mM solutions initially exhibited small aggregates (20 nm), which resulted from the self-assembly of the monomers. After 12 h, a large aggregate (786 nm) was observed in the 10 mM solution of **Mito-1**, while no size change was detected in the case of the 1 mM solution (**Fig. 2c**). The formation of fibrous polymeric structures in the high-concentration solution (10 mM) was confirmed by scanning electron microscopy (SEM) and transmission electron microscopy (TEM) (**Fig. 2d**). These outcomes indicated that the self-assembly during polymerization was induced by the increase in the hydrophobicity of the polymers by the disulfide bonds on the aromatic core, which resulted in a decrease in the entropic penalty.

The above observations suggest that the monomer concentration is important in the processes of disulfide polymerization and polymer self-assembly, particularly in an intracellular reducing environment. To estimate the optimal concentration of the monomer for intracellular PISA at 10 mM GSH, we performed the polymerization at varying concentrations of **Mito-1** (0.1–10 mM) in the presence of a hydrophobic probe, namely Nile red (300 nM). Nile red exhibits no fluorescence in water; however, undergoes fluorescence enhancement in hydrophobic environments. As demonstrated in **Fig. 2e**, a sharp increase was detected at a **Mito-1** concentration of ~2 mM, indicating that PISA can take place above this concentration even in a reducing environment. The progress of the polymerization was further monitored at different monomer concentrations using a solution mimicking the mitochondrial environment. HPLC analysis revealed that no polymer formation was observed in a 1 mM monomer solution; however, construction of large polymers was noted as the concentration was increased to >2 mM (**Fig. 2f, g**). This suggested that in the intramitochondrial environment, a monomer concentration of at least 2 mM was required for the formation of disulfide macromolecules.

As mentioned above, oxidizing agents can act as fuels for the formation of disulfide bonds.³⁹ Thus, it was envisioned that the presence of such compounds would accelerate PISA of **Mito-1** in a reducing environment even at low concentrations of the monomer. In this study, we monitored the consumption of **Mito-1** in the presence of 100 μ M hydrogen peroxide (H_2O_2) as the oxidizing agent using HPLC. No significant changes in the intensity of the peak corresponding to the monomer (1 mM) were observed in the absence of the oxidizer. In contrast, a decrease in the peak intensity was noted following treatment with 100 μ M H_2O_2 (**Fig. S1a**). This implied that the employed oxidizing agent catalyzed the polymerization and PISA (**Fig. S1a, c**). The sizes of the assemblies in 1 and 10 mM solutions of **Mito-1** incubated in the presence of 100 μ M H_2O_2 were determined at 706 and 2308 nm, respectively (**Fig. S1b**).

The addition of 100 μM H_2O_2 lowered the critical concentration of PISA to 1.1 mM (Fig. S1d, e), which was in accordance with the microscopic observations (Fig. S1c).

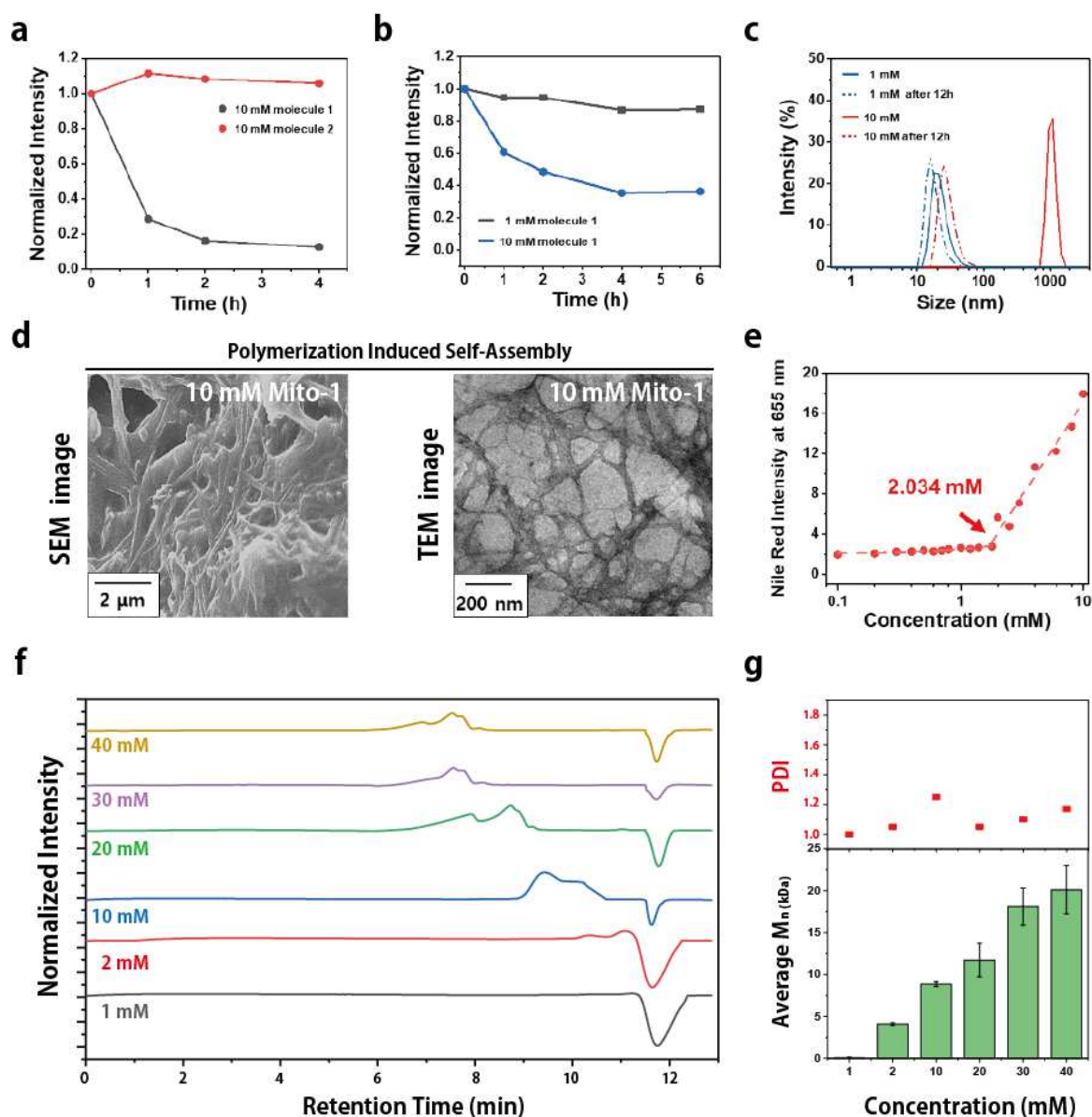


Fig. 2 | Polymerization using disulfide bond and self-assembly. **a**, Time-dependent intensity of the HPLC peaks attributed to **Mito-1** and **Mito-2** (10 mM) in a pH 8.0 buffer solution during polymerization for 4 h. The amounts of **Mito-1** and **Mito-2** were quantified by HPLC and displayed as normalized intensity using the initial intensity. **b**, Time-dependent intensity of the HPLC peaks corresponding to **Mito-1** (1 mM and 10 mM) in a mitochondrial mimic solution (pH 8.0, PBS buffer containing 10 mM GSH) during polymerization for 6 h. The amount of the monomer was quantified by HPLC and displayed as normalized intensity using initial intensity. **c**, Polymerization leads to self-assembly, which results in the formation of a nanostructure. Size distribution of **Mito-1** (1 and 10 mM) in the mitochondrial mimic solution (pH 8.0, PBS buffer containing 10 mM GSH) at 0 and 12 h. The size of the polymeric structure

was analyzed by DLS. **d**, SEM and TEM images of **Mito-1** (1 and 10 mM) after stirring in the PBS buffer (pH 8) containing 10 mM GSH for 24 h. **e**, Critical aggregation concentration determination of **Mito-1** in the PBS buffer (pH 8) containing 10 mM GSH. Steady fluorescence excitation spectra of Nile red at 645 nm and calibration plot obtained based on the emission spectra. **f**, GPC data for the polymerization of **Mito-1** in the PBS buffer (pH 8) containing 10 mM GSH at various concentrations of the monomer (1, 2, 10, 20, 30, and 40 mM). **g**, Quantification of the average molecular weight and PDI values.

Disulfide polymerization and the self-assembly process were further investigated employing a computational method (see section titled **Simulation details**). The possibility of disulfide polymerization was predicted by constructing reaction coordinates using density functional theory (DFT) calculations (**Fig. S2a**). It was found that the formation of a disulfide bond was possible when H₂O₂ was located between two 1,3-benzenedithiol groups. The distance between the hydrogen atom of the thiol group (–SH) and the oxygen atom of H₂O₂ was determined at 2.3 Å. Analysis of the exothermic formation of the disulfide bond showed that the dissociation of H₂O₂ into OH[–] and hydration reaction occurred when the energy barrier was ~20 kcal/mol. Conversely, the scission of the disulfide bond required a large amount of energy (i.e., ~91 kcal/mol). Hence, it was anticipated that the disulfide bond formation would be thermodynamically favorable and stable in the ROS environment. In addition, the promotion of polymerization in the presence of H₂O₂ was evaluated using a molecular dynamics (MD) simulation. Unlike in pure water, at higher concentrations of H₂O₂, the thiol moieties were located in a range of distances (i.e., 3.5–4.7 Å) (**Fig. S2b**) due to the formation of hydrogen bonds (HB) with the oxidizer (**Fig. S2c**). A representative configuration, in which H₂O₂ is located between two thiol groups, is shown in **Fig. S2d**. Thus, based on the theoretical analysis, polymerization through disulfide bonding could be promoted in the ROS environment. Moreover, higher degree of polymerization could be expected at higher H₂O₂ concentrations.

We subsequently investigated whether the degree of polymerization affected the self-assembled structure by varying the polymer chain length using the coarse-grained MD (CGMD) simulation. All long (i.e., 34 constituent monomers) and short (i.e., 5 constituent monomers) polymer chains (**Fig. S3a**) in a high and low ROS environment self-assembled to fibrous (**Fig. 3a**) and spherical structures (**Fig. S3b**), respectively. In both fibrous and spherical structures, the main interactions during the self-assembly process were non-polar interactions between the backbone (BB) groups (**Fig. 3b** and **Fig. S3c**). During the formation of the fibrous structure, the BB groups were entangled along the long chain axis and formed a stacked structure with

the benzene rings (**Fig. 3c**). It was found that long polymerized chains, which hardly bent after a 30% decrease in the end-to-end distance during the initial 20 ns of the self-assembly (**Fig. S4a**), formed net-like stems that turned into a fibrous structure (**Fig. S4b**). During the construction of the net-like stems, the side chain (SC) and TPP groups were positioned at the surface of the fibrous structure (**Fig. 3d**). It is noteworthy that both SC and TPP groups are positively charged; therefore, they are able to target tumor cell membranes. In contrast, in the spherical structure, the BB groups could not interact in the parallel direction due to the insufficient length of the chains (**Fig. S5a**). Thus, the entanglement of BBs along the axis was less likely. Consequently, with the exception of the core, the contents of the three **Mito-1** components (BB, SC, and TPP) were similar throughout the structure (**Fig. S5b**). Accordingly, we anticipated that compared to the spherical assembly, the membrane-interaction ability of the fibrous structure, which was self-assembled by a high degree of polymerization, would be higher due to the exposed TPP and SC groups on the surface.

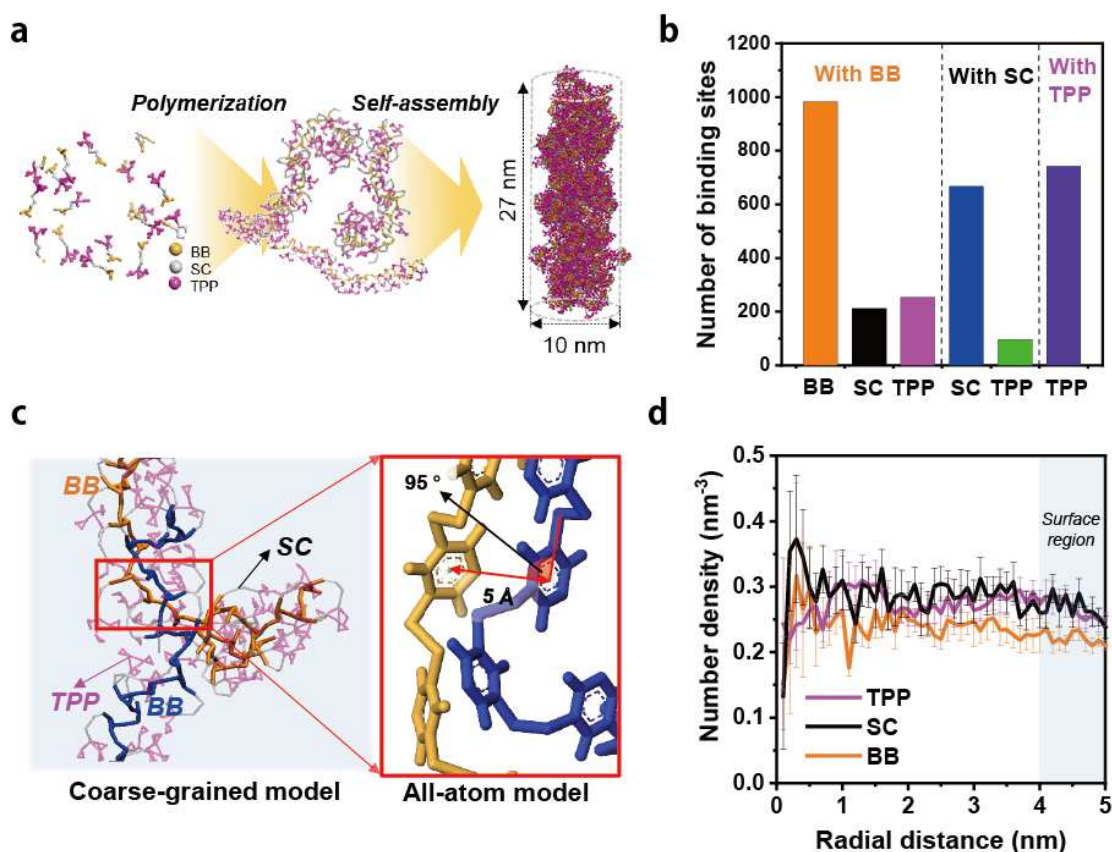


Fig. 3 | Simulation for the fibrous structure. **a**, Scheme showing polymerization and self-assembly of **Mito-1** as well as the self-assembled fibrous structure obtained from the CGMD results. **b**, Number of binding sites between the BB, SC, and TPP groups in the fibrous structure. **c**, Binding states of two polymer chains at the surface of the fibrous structure. Stacking of the BB groups is shown in the red box. The distance and angle of the stacking interaction are also

indicated. **d**, Number density of TPP, SC, and BB in the fibrous polymeric structure between the principal axis of the cylindrical shape to its surface. Surface region in the fibrous structure is indicated in light blue.

Intramitochondrial PISA. The above results indicated that PISA of **Mito-1** required a certain concentration (~ 2 mM) of the monomer and could be accelerated in an oxidative environment. It was hypothesized that mitochondria of cancer cells would be suitable locations for PISA of **Mito-1**, because the TPP moiety could drive the selective localization of the monomers into the organelles with high local concentration.⁴⁰⁻⁴² In addition, ROS are overexpressed in most cancerous mitochondria. Nitrobenzoxadiazole (NBD)-labeled **Mito-1** (**Mito-1-NBD**) and **Mito-2** (**Mito-2-NBD**) were synthesized to investigate the intramitochondrial accumulation of the monomer as well as the subsequent polymerization process (**Fig. 4a**). It was confirmed that **Mito-1-NBD** exhibited green fluorescence with a maximum intensity at 545 nm (**Fig. 4b**). Interestingly, the emission intensity increased 6-fold following polymerization (**Fig. 4c**). Consequently, PISA could be confirmed by the appearance of bright fluorescence inside the cell. NBD displays strong fluorescence in hydrophobic environments; therefore, it could be effectively employed as a reporter for the intracellular assembly.⁴³ Incubation of 30 μ M **Mito-1-NBD** with HeLa cells resulted in weak green fluorescence after 1 h. However, the fluorescence significantly increased after 4 h of incubation. Conversely, the fluorescence of **Mito-2-NBD** remained weak following 4 h of incubation (**Fig. S6a, b**). Confocal laser scanning microscopy (CLSM) revealed that the green fluorescence of **Mito-1-NBD** well overlapped with the red fluorescence of the MitoTracker, which was confirmed by a high Pearson's correlation coefficient (0.806) (**Fig. 4d**).

Moreover, the mitochondrial accumulation of **Mito-1-NBD** was evaluated to establish whether an effective concentration of the monomer inside the organelle could be achieved. **Mito-1-NBD** was incubated with HeLa and HEK293 cells for 4 h, and the emission spectrum was monitored using a mitochondria-isolated solution. The conducted calculations showed that the accumulation of **Mito-1-NBD** inside cancerous mitochondria was consistent with the incubation concentration, i.e., 7.5 ± 1.3 mM and 18.9 ± 2.4 mM for incubation concentrations of 10 and 30 μ M, respectively. Furthermore, the **Mito-1-NBD** accumulation level was >7 times greater in the mitochondria of cancer cells than that in normal cells (**Fig. 4e**). Hence, accumulation of **Mito-1-NBD** provided a critical monomer concentration (1.1 mM) under mitochondria mimicking conditions, which favored the occurrence of polymerization within

the mitochondria of cancer cells at a feeding concentration of 30 μM . The polymerization was further confirmed by GPC after 12 h of incubation in the presence of 30 μM **Mito-1** using cell lysate. The molecular weight of the polymer was determined at 8 kDa and the DPI was calculated at 1.2 (**Fig. 4f**). To verify the importance of mitochondrial localization, we subsequently synthesized TPP-free compounds (**Cyto-1**) as controls (**Fig. S10a**). In the cytosol, abundant reducing agents, such as GSH, promote the destruction of disulfide bonds rather than their generation, preventing polymerization. Expectedly, no polymer formation was observed in the cell lysate treated with 30 μM **Cyto-1** (**Fig. 4g**), suggesting that mitochondria targeting is crucial for the occurrence of disulfide polymerization. To assess the intramitochondrial polymerization in more detail, a TEM experiment was conducted using HeLa cells treated with 30 μM **Mito-1** for 12 h. The obtained TEM images showed disruption of the cellular membrane and the lack of normal mitochondria. Instead, the presence of a fibrous polymeric structure, which penetrated the mitochondrial membrane, was noted (**Fig 4h**). However, the mitochondria in the HEK293 cells treated with **Mito-1** remained unaffected. Thus, it is expected that the presence of a polymeric structure inside the mitochondria of cancer cells could adversely affect mitochondrial function.

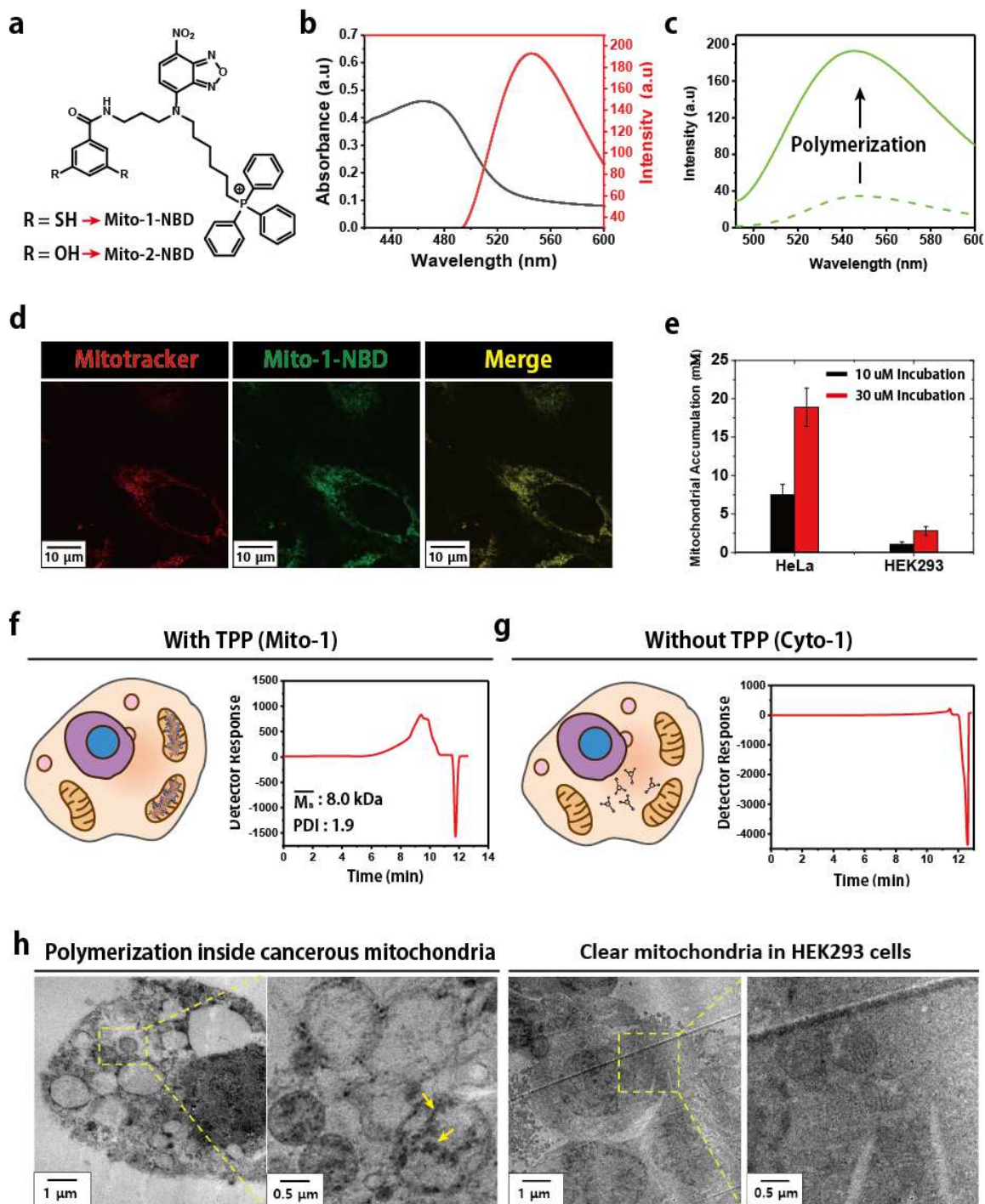


Fig. 4. | Intramitochondrial polymerization **a**, Chemical structures of **Mito-1-NBD** and **Mito-2-NBD**, derivatives of **Mito-1** and **Mito-2**, respectively. **b**, Absorption and emission spectra of **Mito-1-NBD**. **c**, Emission spectra of 100 μM **Mito-1-NBD** (dashed line) and the polymerized product following stirring in the PBS buffer (pH 8) for 24 h (solid line). **d**, CLSM images showing the localization of **Mito-1-NBD** in the mitochondria of HeLa cells. The mitochondria were stained with MitoTracker Deep Red. **e**, Intramitochondrial accumulation of **Mito-1-NBD** in the HeLa and HEK293 cells treated with the conjugate for 4 h. The cells were washed and the mitochondria were isolated. The concentration of **Mito-1-NBD** was quantified by fluorescence measurements. **f** and **g**, GPC traces of intramitochondrial polymerization in

the HeLa cells after 12 h of incubation with 30 μ M **Mito-1** and 30 μ M **Cyto-1**, respectively. The cells were washed and lysed, and the polymers were characterized by GPC. **h**, TEM images of the HeLa and HEK293 cells treated with 30 μ M **Mito-1**.

Intramitochondrial PISA induces mitochondrial dysfunction. It was hypothesized that intramitochondrial polymerization would provide a source of oxidative stress, leading to damage of the mitochondrial function. We initially evaluated the depolarization of the mitochondrial membrane utilizing the JC-1 assay, which emitted red fluorescence under healthy conditions and green fluorescence upon membrane depolarization.⁴⁴ The HeLa cells stained with JC-1 displayed strong red fluorescence in the mitochondria after 1 h of incubation with 30 μ M **Mito-1**, which indicated the presence of healthy organelles. However, after 10 h of incubation, increased green fluorescence was noted in the cells, suggesting that intramitochondrial PISA damaged the mitochondrial membranes (**Fig. 5a**). The mitochondrial membrane damage was further investigated using the tetramethylrhodamine methyl ester (TMRM) assay. It was found that the strong red fluorescence exhibited by the HeLa cells decreased following the treatment with 40 μ M **Mito-1** for 4 h. In contrast, in the case of **Mito-2**, strong fluorescence was observed even after 4 h of incubation (**Fig. S7a**). This implied that the intramitochondrial polymerization of **Mito-1** selectively affected the functionality of the organelle in cancer cells. We proposed that this mitochondrial damage could be attributed to the generation of ROS, which further catalyzed the polymerization. Thus, we performed a ROS assay employing CLSM in the presence of MitoSOX. MitoSOX emits red fluorescence in response to elevated levels of ROS. The conducted ROS assay yielded strong red fluorescence in HeLa cells treated with 30 μ M **Mito-1** for 4 h. Conversely, no red fluorescence was detected in HeLa cells treated with **Mito-2** (**Fig 5b, S7b**). This indicated that polymerization-induced oxidative stress in the mitochondria, which led to the generation of ROS.

The production of ROS driven by the initial polymerization process promoted further autocatalytic polymerization, leading to the construction of bulky polymeric structures and severe damage to the mitochondria. To evaluate the mitochondrial damage, the morphology of these organelles was observed using fluorescence microscopy. A fluorescent Mito-tracker was used to exhibit elongated healthy mitochondria in the HeLa cells after 1 h of incubation with 40 μ M **Mito-1**. Following incubation for 4 h, however, severe mitochondrial fragmentation and swelling were observed (**Fig. 5c**). In contrast, mitochondrial morphology remained unchanged after incubation with **Mito-2** (**Fig. S7c**). It is known that mitochondria play crucial roles in the production of ATP; hence, to investigate the mitochondrial dysfunction in more detail, we

analyzed the cellular ATP levels. It was found that the ATP levels in the HeLa cells treated with **Mito-1** for 24 h decreased by 85% (**Fig. S8a**). Undoubtedly, ATP depletion significantly contributed to cellular dysfunction, causing membrane disruption, protein damage, and cellular death. In this study, the cellular damage was analyzed by monitoring the release of lactate dehydrogenase (LDH), an enzyme released from the cytosol as a result of damage to the plasma membrane. The release of LDH was studied in HeLa and HEK293 cells treated with **Mito-1** for 24 h. A release of LDH of ~80% was confirmed in HeLa cells treated with 50 μ M **Mito-1**, whereas a release only 20% was observed in HEK293 cells (**Fig. S8b**). These outcomes suggested that the fibrous polymers inside mitochondria destroyed the mitochondrial membrane and led to the dysfunction of the organelle.

The penetration of fibrous polymeric structures into the cancer cell membranes was also confirmed by CGMD simulations. It was shown that the fiber reached the center of the lipid bilayer after 1 μ s (**Fig. 5d**). Initially, i.e., within 0–5 ns, the TPP functionality strongly interacted with the surface of the cell membrane, which was composed of negatively-charged hydrophilic phosphate groups (**Fig. 5e**). Due to the interaction of TPP with the membrane surface, the side chain of the molecule was stretched and the angle between BB and TPP increased (**Fig. 5f**). In addition, we found that the TPP group penetrated the cell membrane earlier and deeper than the BB and SC moieties. This was evidenced by the distance of the **Mito-1** components from the center plane of the membrane determined during the simulation (**Fig. 5g**). When the fibrous structure reached the center of the membrane, the TPP moiety mainly interacted with the hydrophobic groups of the membrane. In addition, the interactions between the SC group and the hydrophilic functionalities of the membrane became strong (**Fig. S9**). This indicated that the TPP groups penetrated the membrane first, followed by the SC moieties. Hence, we theoretically predicted that the fibrous polymeric structure allowed the TPP groups to effectively interact with the cancer cell membrane, which was advantageous for targeting and inducing its destruction.

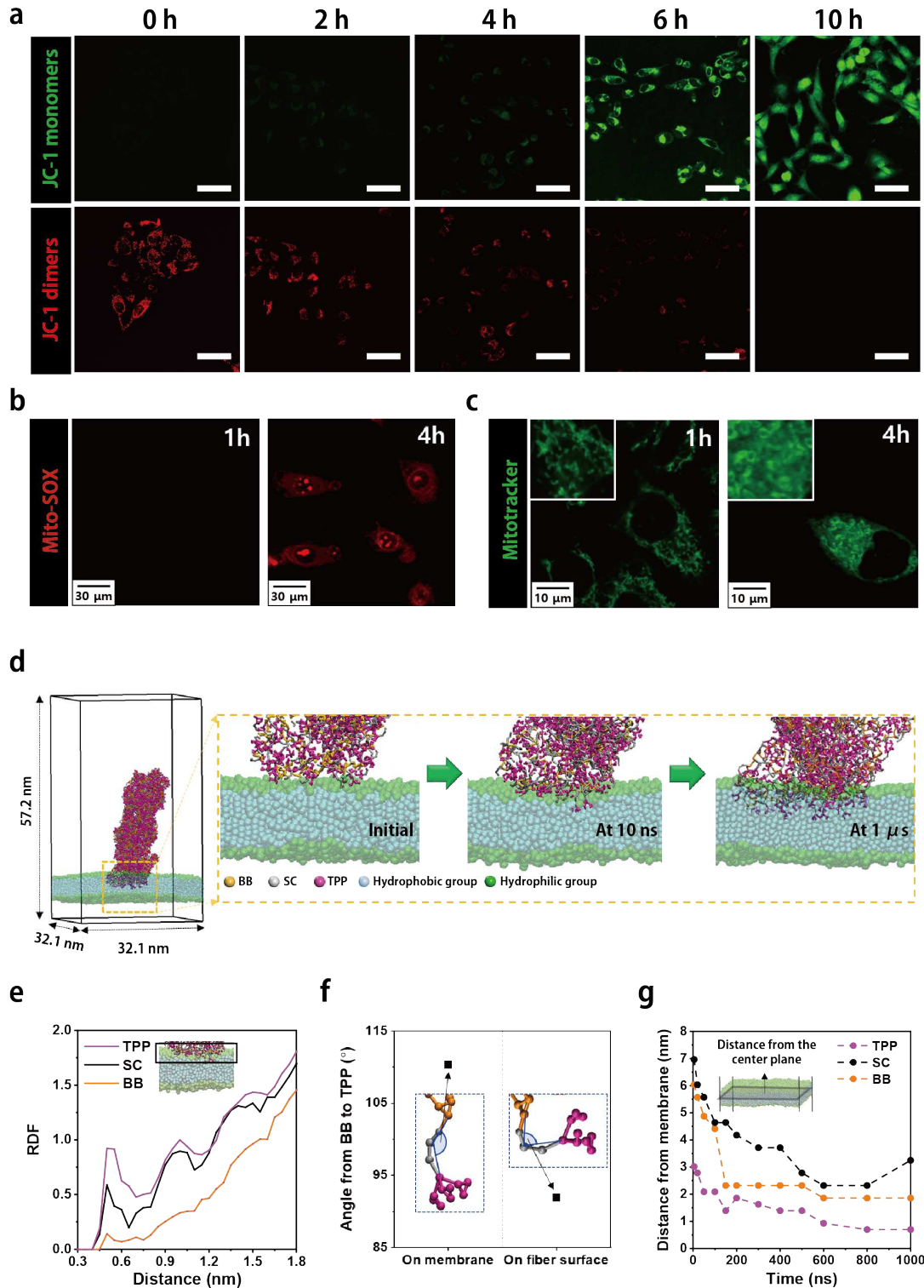


Fig. 5. | Intramitochondrial PISA induces mitochondrial dysfunction. **a**, Membrane depolarization of mitochondria was measured using the JC-1 dye. JC-1-labeled cells were observed by CLSM following treatment with 40 μM **Mito-1** for 10 h. The scale bar is 100 μm . **b**, Confocal analysis showing the generation of ROS using MitoSOX. The HeLa cells were labeled by Mito-SOX after treatment with 40 μM **Mito-1** for 4 h. The intramitochondrial superoxide levels were measured by CLSM. **c**, Confocal microscopy image showing mitochondrial fragmentation following intramitochondrial polymerization. The HeLa cells

were incubated with 40 μ M **Mito-1** for 4 h and the mitochondrial condition was evaluated using MitoTracker green. **d**, The penetration of the fibrous structure into the cancer cell membrane and the penetrated states over the simulation time are shown in the yellow dotted box. Water molecules are omitted for clarity. **e**, Radial distribution function (RDF) of the BB, SC, and TPP moieties as well as of the hydrophilic groups of the lipids in the cell membrane at the initial stage of the penetration. The analyzed region is marked by a black box. **f**, Angles between BB and TPP in the fibrous structure on the cell membrane and on the surface of the fibrous structure. Blue dotted insets show the angles measured between the BB, SC, and TPP groups. **g** Distances of the BB, SC, and TPP moieties from the center of the cell membrane during the simulation.

Intramitochondrial PISA induces cellular necroptosis. It was found that **Mito-1** induced selective mitochondrial dysfunction in cancer cells, specifically in human cervical HeLa cancer cells. The compound did not affect normal cells, i.e., HEK293, human embryonic kidney cells. Based on these results, we expected that intramitochondrial polymerization could be a potential anticancer strategy, as the dysfunction of mitochondria is associated with cellular death. We first examined the toxicity of intramitochondrial polymerization against HeLa and HEK293 cells for 24 h. **Mito-1** exhibited high cytotoxicity against HeLa cells (**Fig. 6a**), while very low toxicity was observed against HEK293 cells, suggesting that **Mito-1** selectively induced cancer cell death (**Fig. 6b**). In contrast, at the same concentration, **Mito-2** displayed almost no toxicity toward both cancer and normal cells (**Fig. 6a, b**). Mitochondria are key organelles responsible for the production of energy. They are also associated with the cellular death mechanisms; therefore, the dysfunction of these organelles significantly affects the intrinsic cell death signaling pathway. Hence, targeting mitochondria would enable cancer therapy with reduced side effects. Notably, such an approach would also prevent drug resistance.²³ We subsequently analyzed the toxicity of **Mito-1** toward various other cancer cell lines, including MDA-MB-468, MDA-MB-231, P-132, and SKBR3. As shown in **Fig. 6c**, **Mito-1** exhibited toxicity toward the investigated cancer cell lines, with IC₅₀ values of 18–28 μ M. Importantly, lower toxicity was observed in the case of normal cell lines (i.e., IMR90 and HEK293) (**Fig. S11**). Furthermore, considering that the mitochondria-targeting strategy might be a promising approach to overcome drug resistance, we tested the cytotoxicity of **Mito-1** toward doxorubicin-resistant cancer cells (MCF7/ADR) after 24 h of incubation. Notably, **Mito-1** displayed higher cytotoxicity than doxorubicin, with an IC₅₀ of 41 μ M (**Fig. S11**). This implied that employing the mitochondria-targeting polymerization system would be an effective strategy to overcome multidrug resistance in cancer treatment.

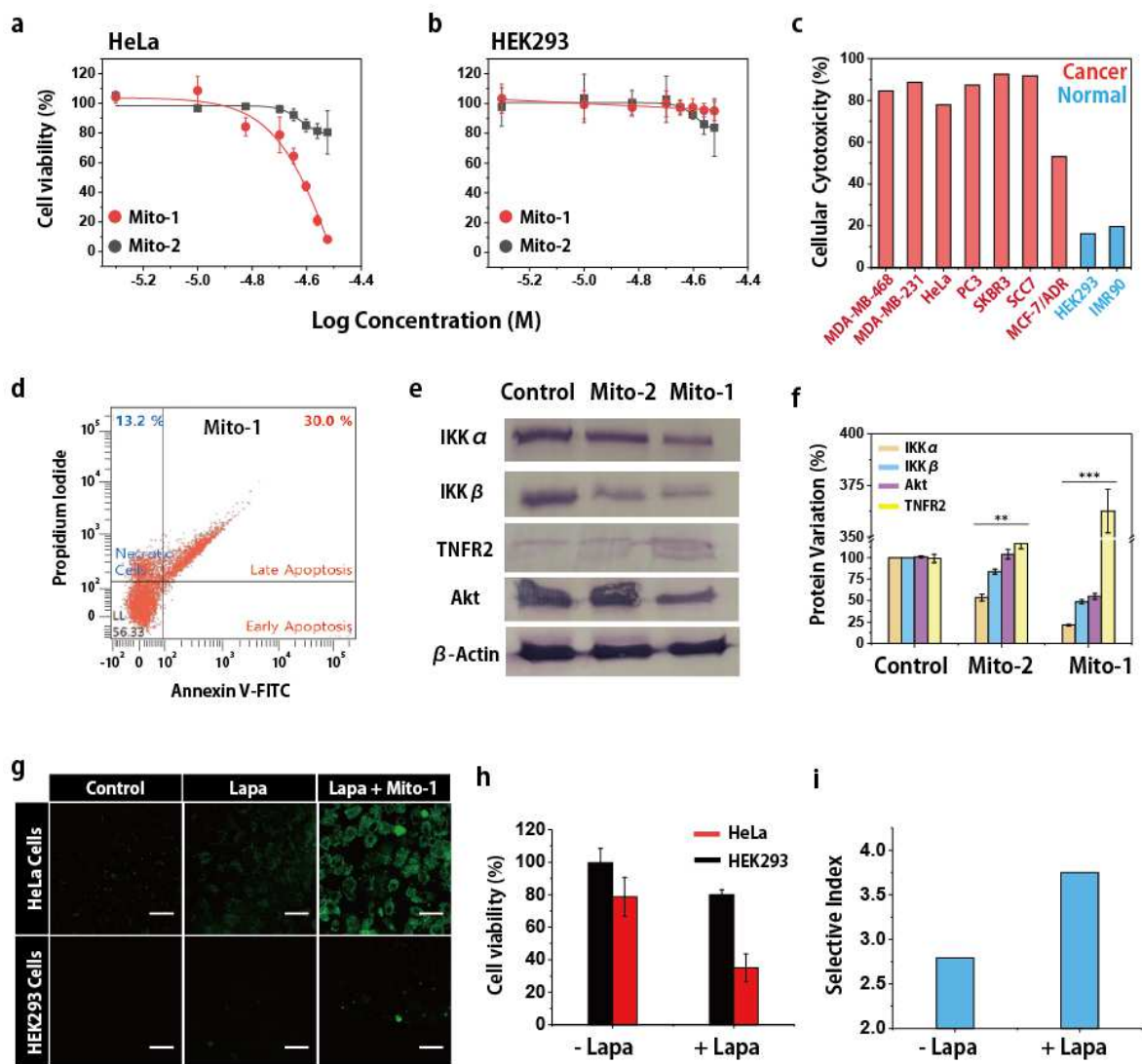


Fig. 6. | Intramitochondrial polymerization for cancer therapy. **a**, HeLa cells and **b**, HEK293 cells were treated with **Mito-1** and **Mito-2** for 24 h and the cellular viability was measured by an MTT assay. **c**, IC₅₀ values of **Mito-1**. Cellular toxicity toward MDA-MB-468, MDA-MB-231, HeLa, PC3, SKBR3, MCF7/ADR, HEK293, and IMR90 cell lines was analyzed. **d**, Flow cytometry analysis showing mitochondria associated necrosis induced by **Mito-1**. **e**, Western blot analysis of necroptotic proteins in HeLa cells treated with **Mito-1** and **Mito-2** for 12 h. The concentration of **Mito-1** and **Mito-2** was 40 μM. **f**, Quantification of protein variation based on western blot analysis. **g**, Fluorescence image showing intracellular ROS in HeLa and HEK293 cells treated with β-lapachone (Lapa) and Lapa + **Mito-1**. The levels of intracellular ROS were measured using the DCFH-DA assay after 4 h of **Mito-1** exposure. **h**, Cytotoxicity of **Mito-1** (20 μM) toward HeLa and HEK293 cells treated with 5 μM Lapa. The analysis showed synergistic effects of the treatment. **i**, Diagram indicating the selectivity index (IC₅₀ of normal cells / IC₅₀ of cancer cells) of synergistic therapy.

To investigate the mechanism of cellular death under these conditions, fluorescence-activated cell sorting analysis was performed utilizing the FITC-annexin V/PI apoptosis detection kit. HeLa cells were treated with 40 μM **Mito-1** for 12 h. It was found that the cells lapsed into the necrosis stage within 12 h (**Fig. 6d, S12**). Moreover, TNF- α , a necrosis related protein, was overexpressed in the cells treated with **Mito-1** (**Fig. S13a**). To examine the cell death mode in more detail, we evaluated the effect of necrostatin-1 (Nec-1), a necroptosis inhibitor, on the cells treated with **Mito-1**.^{45,46} Notably, treatment of these cells with Nec-1 prevented them from cellular death. This suggested that **Mito-1** induced necroptosis, a programmed form of necrosis, in HeLa cells (**Fig. S13b**). Using western blot analysis, we further explored the mechanism of cell death by focusing on the necroptotic signaling pathways of HeLa cells subjected to intramitochondrial polymerization. The cellular stress resulting from **Mito-1** exposure led to elevated expression of TNFR2 and decreased expression of IKK α , IKK β , and Akt (**Fig. 6e, f**). In contrast, incubation of the HeLa cells with **Mito-2** did not have a significant effect on the expression levels of the necroptotic proteins. These outcomes indicated that intramitochondrial polymerization activated cellular death and contributed to the anticancer activity of the monomer. However, an experiment involving treatment of the HeLa cells with **Cyto-1** revealed lack of toxicity after 24 h of incubation, suggesting that mitochondria targeting is essential for disulfide polymerization as well as for effective regulation of the cellular function (**Fig. S10b**).

Intriguingly, the cytotoxicity of **Mito-1** was enhanced after treatment with H₂O₂, which increased the intracellular ROS levels, indicating that polymerization was accelerated in an oxidative environment. As demonstrated in **Fig. S14a**, higher cytotoxic activity was observed in HeLa cells pretreated with 30 μM H₂O₂ for 24 h (IC₅₀ = 17.7 μM) than in cells without any oxidizer pretreatment (IC₅₀ = 22.3 μM) (**Fig. S14a**). However, an opposite trend was observed in the case of cells treated with glutathione monoester (GSH-OMe). It is known that due to its anionic nature, GSH cannot be internalized into cellular membranes. Conversely, neutral GSH-OMe can be incorporated into cells, where it is hydrolyzed to GSH. We found that **Mito-1** exhibited lower toxicity toward cells treated with GSH-OMe (IC₅₀ > 50 μM) (**Fig. S14b**). Inspired by these results, we assumed that a combination of **Mito-1** and β -lapachone (Lapa), a therapeutic agent resulting in the generation of ROS catalyzed by NQO1, would lead to synergistic effects, thus representing an attractive strategy for boosting the efficacy of intramitochondrial polymerization.⁴⁷ As the expression of the NQO1 enzyme in cancer cells is

100 times higher than in normal cells, the use of Lapa could improve the selectivity of the ROS-responsive system.⁴⁷ The ROS assay demonstrated high levels of ROS in HeLa cells treated with 5 μ M Lapa. In contrast, the ROS levels in HEK293 cells remained unchanged after incubation with 5 μ M Lapa (**Fig. 6g**). Lapa significantly enhanced ROS levels in cancer cells, and the corresponding cytotoxicity of **Mito-1** was evidently higher. Combination of **Mito-1** (20 μ M) and 5 μ M Lapa led to a decrease in the cell viability to 35%. In the case of **Mito-1** alone, the cell viability decreased to 78%. It is noteworthy that 80% of normal cells treated with 20 μ M **Mito-1** and 5 μ M Lapa remained unaffected (**Fig. 6h**), which was attributed to the low level of ROS in these cells (**Fig. 6g**). To examine the improved selectivity in more detail, we calculated the selectivity index by dividing the IC_{50} value of the normal cells by the IC_{50} value of the cancer cells. **Mito-1** alone exhibited a low selectivity index of 2.79, whereas treatment with both **Mito-1** and 5 μ M Lapa yielded a higher selective index of 3.75 (**Fig. 6i**). These outcomes demonstrated that such a synergistic strategy could improve the available anticancer treatments.

***In vivo* anticancer effect of intramitochondrial PISA.** We subsequently investigated the *in vivo* therapeutic efficacy of intramitochondrial polymerization by monitoring tumor suppression into nude mice (n = 6 mice per group). Mice exhibiting SCC7 tumors were treated with PBS, Lapa, **Mito-1**, or Lapa+**Mito-1** by intratumoral injection at a dose of 5 mg/kg once every three days (eight injections in total). The antitumor effect of each treatment was monitored by measuring the tumor growth. As shown in **Fig. 7a**, **Mito-1** significantly inhibited the growth of the tumor after 24 days of treatment. In contrast, the treatment with Lapa resulted in comparable tumor growth with that observed in the case of the control. Notably, the anticancer properties of **Mito-1** were enhanced by the synergistic effect of the combination of the monomer with Lapa, which was consistent with the *in vitro* results. On day 24 of the treatment, the decreased size of the tumor could be observed by naked eye. Moreover, the average weight of the tumors in the groups treated with control, Lapa, **Mito-1**, and Lapa+**Mito-1** was measured at 4.1, 3.9, 2.1, and 1.8 g, respectively (**Fig. 7b, c**). In the control group, 60% of the mice died within 45 days. An obvious improvement of the mice survival was observed for the **Mito-1** and Lapa+**Mito-1** groups (**Fig 7d**). This suggested that the intramitochondrial polymerization resulted in significant anticancer effects. Administration of **Mito-1** and Lapa+**Mito-1** did not induce any noticeable changes in the mice body weight, indicating that

the intramitochondrial polymerization was tolerated by the animals (**Fig. 7e**). In addition, we evaluated the cell morphology by staining the cells with hematoxylin and eosin using the TUNEL assay to investigate the mode of cell death. Both control- and Lapa-treated groups exhibited no damage in the tumor section. Necrosis was observed in **Mito-1**- and Lapa+**Mito-1**-treated groups (**Fig 7f, g**). Furthermore, histopathology of other organs revealed negligible toxicity resulting from intramitochondrial polymerization *in vivo* (**Fig. S15**). Overall, we successfully demonstrated that intramitochondrial PISA led to anticancer effects. Notably, combination of the synthesized monomer with Lapa resulted in promising synergistic effects.

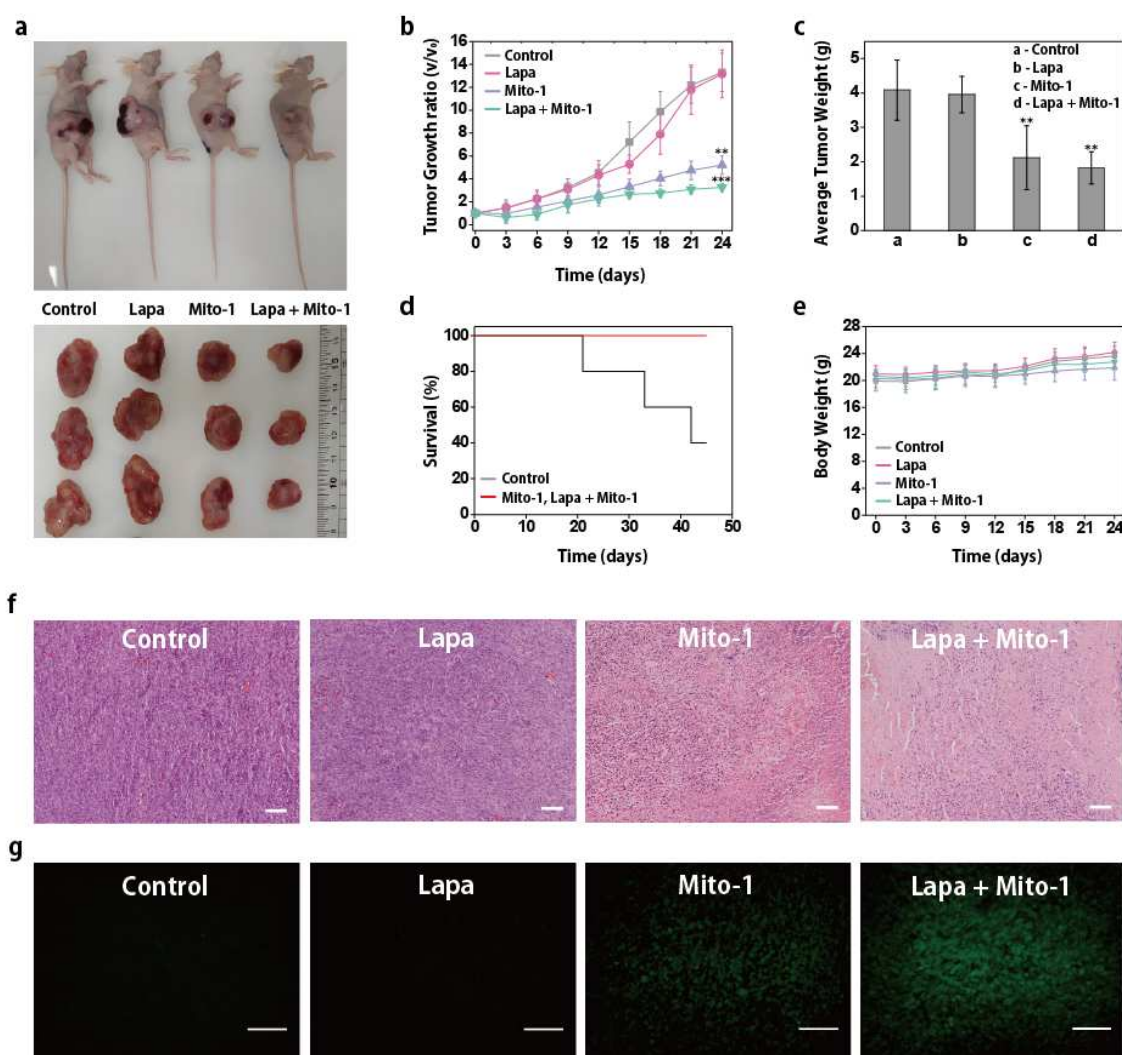


Fig. 7. | Anticancer efficacy of intramitochondrial polymerization. a, Images of mice and tumors after 24 days of treatment (n=6 per group). The dose of the **Mito-1** and Lapa injections was 5 mg kg⁻¹. **b**, Observation of the tumor inhibitory effects in the control, Lapa, **Mito-1**, and Lapa+**Mito-1** treatment groups. **c**, Weight analysis of the tumors collected after treatment for 24 days. **d**, Cumulative survival of different treatment groups exhibiting SCC7 tumors. All mice receiving **Mito-1** and Lapa+**Mito-1** treatment survived for 45 days. **e**, Weight change of

the mice in the tumor model after 24 days of treatment (n = 10 per group) The dose of the Mito-1 and Lapa injections was 5 mg kg⁻¹. **f**, Hematoxylin and eosin staining and **g**, TUNEL assay of tumor sections treated with control, Lapa, **Mito-1**, and Lapa+**Mito-1** for 24 days. The experiments were repeated three times and representative images are shown in the figure. Scale bar is 100 μm.

Conclusion

In the present study, intramitochondrial polymerization using disulfide bonds was achieved for the first time as a potential anticancer therapy. At high concentration, the designed **Mito-1** monomer caused disulfide polymerization even in a reducing environment. Moreover, self-assembly of the resulting polymers led to the formation of structured macromolecules. TPP groups in **Mito-1** drove the accumulation of the monomer inside cancerous mitochondria, resulting in the construction of fibrous polymeric structures. Intramitochondrial polymerization-induced depolarization of the mitochondrial membrane and generation of ROS. In addition, increased oxidant-catalyzed polymerization was also observed. This led to mitochondrial damage, resulting in the mitochondrial-mediated necrosis of cancer cells. Furthermore, combination of **Mito-1** with Lapa, an agent increasing the levels of intracellular ROS, resulted in synergistic effects. The formation of disulfide polymers inside cells enables establishment of artificial systems, which can control the fate of cells utilizing intracellular machinery. The approach described herein could potentially be used to regulate chemical processes inside cells as well as to explore the fundamental cellular mechanisms.

General methods and materials. Methyl 3,5-dihydroxybenzoate was purchased from Alfa Aesar (UK). Dimethylthiocarbamoyl chloride was obtained from Sigma-Aldrich (USA). Diphenyl ether, triphenylphosphine, dibromopropane, *N,N*-dimethyl-1,3-propanediamine, and potassium hydroxide were acquired from TCI (Japan). All products were purified by HPLC (Agilent Technologies, USA) equipped with a C18 reverse phase column. TMRM was obtained from Santa Cruz Biotechnology (USA). MitoSox, dihydroethidium (DHE), MitoTracker green, MitoTracker red FM, annexin V, propidium iodide (PI), and Alexa Fluor were purchased from Life Technologies (USA). The successful synthesis of the product was confirmed with matrix-assisted laser desorption/ionization-time of flight (MALDI-TOF/TOF) mass spectrometry, electrospray ionization mass spectrometry (ESI-MS), and nuclear magnetic resonance (NMR). The CLSM images were taken using the LSM 7800 and FV 1000 confocal microscopes. The

TEM images were obtained employing a BioTEM system (JEM 1400).

Cell culture. Human cancer cells originating from the cervix (HeLa), breast (MDA-MB-468, MDA-MB-231, and SKBR3), and prostate (PC3), as well as noncancerous fibroblast cells (HEK293 and IMR90), were cultured in Dulbecco's Modified Eagle Medium (DMEM) and RPMI (Life Technologies) containing 10% fetal bovine serum (FBS) (Life Technologies) and 1% penicillin/streptomycin (Life Technologies) at 37 °C in a humidified atmosphere of 10% CO₂. For the cytotoxicity analysis, the cells were cultured in the presence of different concentrations of the Mito-1 and Mito-2 (0, 5, 10, 20, 30, 50, 60, 80, and 100 μM). The cell viability was measured after 24 h using the MTT assay. All data points were measured in quadruplicate. Fluorescence measurements were conducted by observing the absorbance at 595 nm emission using a microplate reader (SpectraMAX 384). 96-well Nunc (Thermo Fisher Scientific, USA) plates were seeded with cells at a density of 4×10^3 cells/well. The cells were allowed to settle by incubation at 37 °C under 5% CO₂ in the respective growth medium for 24 h.

Imaging of mitochondrial depolarization. HeLa and HeK293T cells were seeded on a Lab Tek II slide chamber at 80% confluence in DMEM (Life Technologies) supplemented with 10% FBS and 1% penicillin/streptomycin. The cells were incubated at 37 °C under 5% CO₂ for 24 hours. Following incubation in the presence of 20 μM of the Mito-1 according to the manufacturer's protocol (JC-1, M34152), the cell culture medium was replaced with a 2 μM JC-1 working solution to cover the adherent cells. The cells were subsequently incubated for 15–30 min at 37 °C in the dark. The cells were gently washed with PBS prior to analysis using FV1000 CLSM. Similarly, to evaluate the mitochondrial membrane depolarization, the TMRM assay was performed according to the manufacturer's instructions (Thermo Fisher Scientific, I34361).

Imaging of ROS generation in cells. The HeLa and HeK293T cells were seeded on a Lab Tek II slide chamber at 80% confluence in DMEM (Life Technologies) supplemented with 10% FBS and 1% penicillin/streptomycin. The cells were incubated at 37 °C under 5% CO₂ for 24 hours. Following incubation in the presence of 20 μM of the molecule according to the manufacturer's protocol (MitoSox, M36008), the cell culture medium was replaced with a 10 μM MitoSox working solution to cover the adherent cells. The cells were subsequently incubated for 15 min at 37 °C in the dark. The cells were gently washed with PBS prior to the analysis using FV1000 CLSM. Accordingly, the DHE and 2',7'-dichlorofluorescein diacetate

assay was performed to evaluate the ROS generation using the method provided by the manufacturer (Thermo Fisher Scientific).

Flow cytometry analysis. The HeLa cells were seeded in a 25 mL T-flask (Thermo Fisher Scientific) in DMEM (Life Technologies) supplemented with 10% FBS and 1% penicillin/streptomycin at 37 °C under 5% CO₂. The cells were incubated with 30 μM of the Mito-1 for 12 h. The cells were then harvested and washed with cold PBS. According to the manufacturer's protocol (Life Technologies, V13241), the cells were incubated with 5 μL of Alexa Fluor 488-conjugated annexin V and 1 μL of a 100 μg/mL PI working solution in 100 μL of the annexin-binding buffer for 15 min at room temperature. Following incubation, 400 μL of the annexin-binding buffer was added with gentle mixing, and the samples were kept on ice. The stained cells were subsequently analyzed by flow cytometry (FACSealibur, BD Biosciences, USA). The fluorescence emission was measured at 530 nm (i.e., FL1) and >575 nm (i.e., FL3).

Western blotting. The HeLa cells were seeded in 6-well plates at a density of 5×10^5 cells/well in DMEM overnight. The cells were then treated with **Mito-1** (20 μM) or **Mito-2** (20 μM) for 24 h. The control wells were not treated with either compound. The cells were lysed with the RIPA buffer and the total protein concentration was determined using the Bradford assay. The proteins were separated using SDS-PAGE and transferred onto a polyvinylidene difluoride (PVDF) membrane (Immobilon-P polyvinylidene fluoride membranes, Millipore Corporation, USA). The PVDF membrane was blocked using skim milk to minimize nonspecific interactions. The membrane was subsequently treated with primary antibodies overnight, and then with secondary antibodies for 2 h. The protein expression was visualized using the 5-bromo-4-chloro-3-indolyl phosphate (BCIP)/nitro blue tetrazolium solution.

Analysis of the anticancer effects. All animal experiments were conducted using a protocol approved by the Institutional Animal Care and Use Committee of the Ulsan National Institute of Science and Technology.

Simulation details. *Density functional theory (DFT).* The DFT calculations were performed to elucidate the mechanism of the disulfide bond formation and dissociation in the 1,3-benzenedithiol moiety in **Mito-1** using the DMol³ software.^{48,49} To evaluate the disulfide bond formation, two 1,3-benzenedithiol groups with two H₂O₂ molecules were analyzed. To

calculate the transition states (TS), complete single linear synchronous transit (LST) and quadratic synchronous transit methods were employed.^{50,51} The convergence criterion of the root mean square force was 0.002 Ha/Å. To optimize the geometry of each state, generalized gradient approximation (GGA) with the Perdew–Burke–Ernzerhof (PBE) functional was used.⁵² Semi-empirical dispersion correction was conducted employing the Tkatchenko–Scheffler approach.⁵³ In addition, spin-polarized calculations using the DNP 4.4 basis set were performed. The convergence criteria for the geometry optimization were 1.0×10^{-5} Ha for energy, 0.002 Ha/Å for force, and 0.005 Å for displacement. The COnductor-like Screening Model (COSMO) method with a dielectric constant of water ($\epsilon = 78.54$) was used to evaluate the electrostatic contribution under hydrated conditions.⁵⁴

Molecular dynamics (MD). The MD simulation was performed analyze the changes in the structure of **Mito-1** according to the concentration of H₂O₂. The systems exhibiting a H₂O₂ concentration of 3.4 wt%, 10 wt%, and 20 wt% included 6, 18, and 36 H₂O₂ molecules, respectively, and 12 **Mito-1** molecules in boxes of $50 \times 50 \times 50 \text{ \AA}^3$. The pure water system included 214 water and 12 **Mito-1** molecules. All MD systems contained the same number of atoms. The NPT MD (i.e., isothermal-isobaric) simulation was performed for 500 ps and the temperature was increased from 300 to 400 K in 10 K intervals. The cycle was repeated 5 times. Subsequently, the NPT simulation was performed for 1 ns at 300 K. COMPASS II force field⁵⁵ was used and the Mulliken charge was applied to 1,3-benzenedithiol and H₂O₂. To maintain the isothermal state, a velocity rescaling thermostat was employed with a time step of 1 fs. The radial distribution function (RDF) was analyzed using the trajectories of the final 500 ps and the number of hydrogen bonds was counted based on 5 trajectories of the final 100 ps.

Coarse-grained molecular dynamics (CGMD). The coarse-grained polymer model was composed of 5 or 34 constituent monomers. The molecular weight was ~2.9 and ~20 kDa, respectively. The MARTINI force field was applied, and the bead types for each CG bead are summarized in **Table SX1**.⁵⁶ For the simulation of the self-assembly of the fibrous polymeric structure, 40 polymer chains were used in a box of $40 \times 40 \times 40 \text{ nm}^3$ filled with water and chlorine ions. To consider the self-assembly following polymerization, in the initial state, the monomers in each chain were connected by distances of $>1.5 \text{ nm}$. The number of water beads was 11,200 and the concentration of the **Mito-1** polymer was 8.99 wt%. Sequential NVT and NPT simulations were conducted at 298 K for 300 ps and 100 ps, respectively, and the polymer was aggregated to a fibrous structure. To confirm the maintenance of the fibrous structure,

water beads were added around the structure and the concentration of the **Mito-1** polymer was 2.97 wt%. The NPT simulation was performed for 15 ns and the temperature was increased from 300 to 400 K in 20 K intervals. The cycle was repeated 3 times. The NPT simulation was then performed for 300 ns at 300 K. The process of self-assembly of the spherical structure and the concentration of **Mito-1** were same as those used for the fibrous structure. The number of short polymer chains consisting of 5 monomers was 272 and a box with the dimensions of $23 \times 23 \times 23 \text{ nm}^3$ filled with water and chlorine ions was used for the simulation. For polymer aggregation, the NPT simulation was performed for 150 ns at 300 K. To confirm the preservation of the spherical structure, water beads were added around the macromolecule and the same sequential simulation as that for the fibrous structure was performed. The number density of the three **Mito-1** components was analyzed using 5 trajectories of the final 25 ns. In addition, the number of binding sites in the fibrous structure was determined using a distance between the particles of $<0.5 \text{ nm}$. The number of binding sites and the length of the side chain were evaluated using the trajectories of the final 10 ns.

Simulation of the fibrous polymeric structure on a cancer cell membrane was performed in a box with the dimensions of $32.4 \times 32.4 \times 56 \text{ nm}^3$ filled with water. The fibrous structure was located on the cell membrane, which was constructed using 3092 molecules of DPPC and 1324 molecules of DPPG in a 2.3:1 ratio. The DPPC and DPPG lipids contain hydrophilic groups (i.e., PO_4^- , $\text{N}^+\text{C}_3\text{H}_9$, $\text{C}(\text{OH})_2\text{H}_3$) and hydrophobic alkyl moieties. The NPT simulations were performed for 1000 ns at 310 K and the RDF analyses were conducted using the trajectories of the initial and final 5 ns. The angles between BB and TPP were measured using the molecules located near the cell membrane and the surface of the fibrous structure. The analysis was performed based on the trajectories of the final 50 ns. The distance from the center of the membrane was determined from the distance between the position, at which the number density of **Mito-1** was over 0.1 nm^{-3} , and the center of the lipid bilayer in the perpendicular direction from the membrane.

All CGMD simulations were conducted at a time step of 10 fs. A velocity rescaling thermostat and Parrinello–Rahman barostat were used for the isothermal-isobaric state. The cut-off radius for van der Waals interactions was 1.2 nm. The particle mesh Ewald method was used to analyze coulomb interactions. The GROMACS 5.0.6 package was used for all CGMD simulations.⁵⁷

References

- 1 Ishikawa, H., Ma, Z., Barber, G. N. STING regulates intracellular DNA-mediated, type I interferon-dependent innate immunity. *Nature* **461**, 788-792 (2009)
- 2 Hornung, V., Latz, E. Intracellular DNA recognition. *Nat. Rev. Immunol.* **10**, 123-130 (2010)
- 3 Jo, D., Liu, D., Yao, S., Collins, R. D., Hawiger, J. *Nat. Med.* **11**, 892-898 (2005)
- 4 Bromberg, J., Darnell, J. E. The role of STATs in transcriptional control and their impact on cellular function. *Oncogene* **19**, 2468-2473 (2000)
- 5 Kushwaha, M., Rostain, W., Prakash, S., Duncan, J. N., Jaramillo, A. Using RNA as molecular code for programming cellular function. *ACS Synth. Biol.* **5**, 795-809 (2016)
- 6 Weisbrich, A., Honnappa, S., Jaussi, R., Okhrimenko, O., Frey, D., Jelesarov, I., Akhmanova, A., Steinmetz, M. O. Structure-function relationship of CAP-Gly domains. *Nat. Struct. Mol. Biol.* **14**, 959-967 (2007)
- 7 Cunnligham, J. M., Koytger, G., Sorger, P. K., AlQuaralshi, M. Biophysical prediction of protein-peptide interactions and sigaling networks using machine learning. *Nat. Methods* **17**, 175-183 (2020)
- 8 Freemanm, R., Han, M., Alvarez, Z., Lewis, J. A., Wester, J. R., Stephanopoulos, N., McClendon, M. T., Lynsky, C., Godbe, J. M., Sangji, H., Luiten, E., Stupp, S. I. Reversible self-assembly of superstructured networks. *Science* **362**, 808-813 (2018)
- 9 Brodin, J. D., Smith, S. J., Carr, J. R., Tezcan, F. A. Designed, helical protein Nanotubes with variable deiameters from a single building block. *J. Am. Chem. Soc.* **137**, 10468-10471 (2015)
- 10 Shigemitsu, H., Kubota, R., Nakamura, K., Matsuzaki, T., Minami, S., Aoyama, T., Urayama, K., Hamachi, I. Protein-responsive protein release of supramolecular/polymer hydrogel composite integrating enzyme activation systems. *Nat. Commun.* **11**, 3859 (2020)
- 11 Kumar, M., Ing, N. L., Narang, V., Wijerathne, N. K., Hochbaum, A. I., Ulijin, R. V. Amino-acid-encoded biocatalytic self-assembly enables the formation of transient conducting nanostructures. *Nat. Chem.* **10**, 696-703 (2018)
- 12 Wang, F., Su, H., Lin, R., Chakroun, R. W., Monroe, M. K., Wang, Z., Porter, M., Cui, H. Supramolecular tubustecan hydrogel as chemotherapeutic carrier to improve tumor penetration and local treatment efficacy. *ACS Nano* **14**, 10083-10094 (2020)

- 13 Cong, Y., Ji, L., Gao, Y. J., Liu, F. H., Cheng, D. B., Hu, Z., Qiao, Y., Wang, H. Microenvironment-induced in situ self-assembly of polymer-peptide conjugates that attack solid tumors deeply. *Angew. Chem. Int. Ed.* **58**, 4632-4637 (2019)
- 14 Wang, H., Feng, Z., Tan, W., Xu, B. Assemblies of D-peptides for targeting cell nucleolus. *Bioconjugate Chem.* **30**, 2528-2532 (2019)
- 15 Wang, H., Feng, Z., Wang, Y., Zhou, R., Yang, Z., Xu, B. Integrating enzymatic self-assembly and mitochondria targeting for selectively killing cancer cells without acquired drug resistance. *J. Am. Chem. Soc.* **138**, 16046-16055 (2016)
- 16 Hai, Z., Ni, Y., Saimi, D., Yang, H., Tong, H., Zhong, K. γ -Glutamyltranspeptidase-triggered intracellular gadolinium nanoparticle formation enhances the T2-weighted MR contrast of tumor. *Nano Lett.* **19**, 2428-2433 (2019)
- 17 Wang, Y., Du, W., Zhang, T., Zhu, Y., Ni, Y., Wang, C., Raya, F. M. S., Zou, L., Wang, L., Liang, G. A self-evaluating photothermal therapeutic nanoparticle. *ACS Nano* **14**, 9585-9593 (2020)
- 18 Son, J., Kalafatovic, D., Kumar, M., Yoo, B., Cornejo, M. A., Contel, M., Ulijin, R. V. Customizing morphology, size, and response kinetics of matrix metalloproteinase-responsive nanostructures by systematic peptide design. *ACS Nano* **13**, 1555-1562 (2019)
- 19 Su, H., Zhang, W., Wang, H., Wang, F., Cui, H. Paclitaxel-promoted supramolecular polymerization of peptide conjugates. *J. Am. Chem. Soc.* **141**, 11997-12004 (2019)
- 20 Mann, S. Self-assembly and transformation of hybrid nano-objects and nanostructures under equilibrium and non-equilibrium conditions. *Nat. Mater.* **8**, 781-792 (2009)
- 21 Karagoz, B., Esser, L., Duong, H. T., Basuki, J. S., Boyer, C., Davis, T. P. Polymerization-induced self-assembly (PISA)- control over the morphology of nanoparticles for drug delivery applications. *Polym. Chem.* **5**, 350-355 (2014)
- 22 Six, J. L., Ferji, K. Polymerization induced self-assembly: an opportunity toward the self-assembly of polysaccharide-containing copolymers into high-order morphologies. *Polym. Chem.* **10**, 45-53 (2019)
- 23 Ladmiral, V., Semsarilar, M., Canton, I., Armes, S. P., Polymerization-induced self-assembly of galactose-functionalized biocompatible diblock copolymers for intracellular delivery. *J. Am. Chem. Soc.* **135**, 13574-13581 (2013)
- 24 Khor, S. Y., Quinn, J. F., Whittaker, M. R., Truong, N. P., Davis, T. P. Controlling

- nanomaterial size and shape for biomedical applications via polymerization-induced self-assembly. *Macromol. Rapid Commun.* **40**, 1800438-1800459 (2019)
- 25 Ma, X., Che, H., Yang, L., Wang, K., Guo, Y., Yuan, L. Construction and potential applications of a functionalized cell with an intracellular mineral scaffold. *Angew. Chem. Int. Ed.* **50**, 7414-7417 (2011).
- 26 El-said, W. A., Cho, H. Y., Yea, C. H., Choi, J. W. Synthesis of metal nanoparticles inside living human cells based on the intracellular formation process. *Adv. Mater.* **26**, 910-918 (2014)
- 27 Geng, J., Li, W., Zhang, Y., Thottappillil, N., Clavadetscher, J., Lilienkamp, A., Bradley, M. Radical polymerization inside living cells. *Nat. Chem.* **11**, 578-586 (2019)
- 28 Peng, B., Zhao, X., Yang, M. S., Li, L. L. Intracellular transglutaminase-catalyzed polymerization and assembly for bioimaging of hypoxic neuroblastoma cells. *J. Mater. Chem. B* **7**, 5626-5632 (2019)
- 29 Komaromy, D., Stuart, M. C. A., Santiago, G. M., Tezcan, M., Krasnikov, V. V., Otto, S. Self-assembly can direct dynamic covalent bond formation diversity or specificity. *J. Am. Chem. Soc.* **139**, 6234-6241 (2017)
- 30 Mattia, E., Otto, S. Supramolecular systems chemistry. *Nat. Nanotechnol.* **8**, 781-792 (2009)
- 31 Liu, B., Pappas, C. G., Ottele, J., Schaeffer, G., Jurissek, C., Pieters, P. F., Altay, M., Maric, I., Stuart, M. C. A., Otto, S. Spontaneous emergence of self-replicating molecules containing nucleobases and amino acids. *J. Am. Chem. Soc.* **142**, 4184-4192 (2020)
- 32 Han, M., Vakili, M. R., Abyaneh, H. S., Molavi, O., Lai, R., Lavasanifar, A. Mitochondrial delivery of doxorubicin via triphenylphosphine modification for overcoming drug resistance in mda-md-435/dox cells. *Mol. Pharmaceutics* **11**, 2640-2649 (2014)
- 33 Zielonka, J., Joseph, J., Sikora, A., Hardy, M., Ouari, O., Vivar, J. V., Cheng, G., Lopez, M., Kalyanaraman, B. Mitochondria-targeted triphenylphosphonium-based compounds: syntheses, mechanisms of action, and therapeutic and diagnostic applications. *Chem. Rev.* **117**, 10043-10120 (2017)
- 34 Cho, D. Y., Cho, H., Kwon, K., Yu, M., Lee, E., Huh, K. M., Lee, D. H., Kang, H. C. Triphenylphosphonium-conjugated poly(ϵ -caprolactone)-based self-assembled nanostructures as nanosized drugs and drug delivery carriers for mitochondria-targeting

- synergistic anticancer drug delivery. *Adv. Funct. Mater.* **25**, 5479-5491 (2015)
- 35 Xu, X., Saw, P. E., Tao, W., Li, Y., Ji, X., Bhasin, S., Liu, Y., Ayyash, D., Rasmussen, J., Huo, M., Shi, J., Farokhzad, O. C. ROS-responsive polyprodrug nanoparticles for triggered drug delivery and effective cancer therapy. *Adv. Mater.* **29**, 1700141-1700147 (2017).
- 36 Jager, E., Hocherl, A., Janouskova, O., Jager, A., Hruby, M., Konefal, R., Netopilik, M., Panek, J., Sluof, M., Ulbrich, K., Stepanek, P. Fluorescent boronate-based polymer nanoparticles with reactive oxygen species (ROS)-triggered cargo release for drug-delivery application. *Nanoscale* **8**, 6958-6963 (2016).
- 37 Chali, S. P., Ravoo, B. J. Polymer nanocotainers for intracellular delivery. *Angew. Chem. Int. Ed.* **59**, 2962-2972 (2020)
- 38 Zhu, C. N., Zang, L. Y., Zheng, D. Y., Cao, H. M., Liu, X. J. Small-sized copolymeric nanoparticles for tumor penetration and intracellular drug release. *Chem. Commun.* **56**, 2000-2003 (2020)
- 39 Creners, C. M., Jakob, U. Oxidant sensing by reversible disulfide bond formation. *J. Biol. Chem.* **288**, 26489-26496 (2013)
- 40 Kim, S., Palanikumar, L., Choi, H., Jeena, M. T., Kim, C., Ryu, J. H. Intra-mitochondrial biomineralization for inducing apoptosis of cancer cells. *Chem. Sci.* **9**, 2474-2479 (2018)
- 41 Jeena, M. T., Jeong, K., Go, E. M., Cho, Y., Lee, S., Jin S., Hwang, S. W., Jang, J. H. Kang, C. S., Band, W. Y., Lee, E. Kwak, S. K., Kim, S., Ryu, J. H. Heterochiral assembly of amphiphilic peptides inside the mitochondria for supramolecular cancer therapeutics. *ACS Nano* **13**, 11022-11033 (2019)
- 42 Jeena, M. T., Palanikumar, L., Go, E. M., Kim, I., Kang, M. G., Lee, S., Park, S., Choi, H., Kim, C., Jin, S. M., Bae, S. C., Rhee, H. W., Lee, E., Kwak, S. K., Ryu, J. H. Mitochondria localization induced self-assembly of peptide amphiphiles for cellular dysfunction. *Nat. Commun.* **8**, 26 (2017)
- 43 Mei, L., He, S., Zhang, L., Xu, K., Zhong, W. Supramolecular self-assembly of fluorescent peptide amphiphiles for accurate and reversible pH measurement. *Org. Biomol. Chem.* **17**, 939-944 (2019).

- 44 Perelman, A., Wachtel, C., Cohen, M., Haupt, S., Shapiro, H., Tzur, A. JC-1: alternative Excitation wavelengths facilitate mitochondrial membrane potential cytometry. *Cell Death Dis* **3**, e430 (2012)
- 45 Zhou, J., Du, X., Chen, X., Wang, J., Zhou, N., Wu, D., Xu, B. Enzymatic self-assembly confers exceptionally strong synergism with NF- κ B targeting for selective necroptosis of cancer cells. *J. Am. Chem. Soc.* **140**, 2301-2308 (2018)
- 46 Cogswell, P. C., Kashatus, D. F., Keifer, J. A., Guttridge, D. C., Reuther, J. Y., Bristow, C., Roy, S., Nicholson, D. W., Baldwin, A. S. NF- κ B and I κ B α are found in the mitochondria. *J. Biol. Chem.* **278**, 2963-2968 (2003)
- 47 Ye, M., Han, Y., Tang, J., Piao, Y., Liu, X., Zhou, Z., Gao, J., Rao, J., Shen, Y. A tumor-specific caspase amplification drug release nanoparticle for overcoming multidrug resistance in cancers. *Adv. Mater.* **29**, 1702342-1702352 (2017)
- 48 Delley, B. An all-electron numerical method for solving the local density functional for polyatomic molecules. *J. Chem. Phys.* **92**, 508-517 (1990)
- 49 Delley, B. From molecules to solids with the DMol³ approach. *J. Chem. Phys.* **113**, 7756-7764 (2000)
- 50 Bell, S., Crighton, J. S. Locating transition states. *J. Chem. Phys.* **80**, 2464-2475 (1984)
- 51 Halgren, T. A., Lipscomb, W. N. The synchronous-transit method for determining reaction pathways and locating molecular transition states. *Chem. Phys. Lett.* **49**, 225-232 (1977)
- 52 Perdew, J. P., Burke, K., Ernzerhof, M. Generalized Gradient Approximation Made Simple. *Phys. Rev. Lett.* **77**, 3865-3868 (1996)
- 53 Tkatchenko, A., Scheffler, M. Accurate Molecular Van Der Waals Interactions from Ground-State Electron Density and Free-Atom Reference Data. *Phys. Rev. Lett.* **102**, 073005 (2009)
- 54 Klamt, A., Schuurmann, G. Cosmo: A New Approach to Dielectric Screening in Solvents with Explicit Expressions for the Screening Energy and its Gradient. *J. Chem. Soc., Perkin Trans. 2.* 799-805 (1993)
- 55 Huai, S., Zhao, J., Chunwei, Y., Reinier, L. C. A., Struan, H. R., Neil, A. S., Simon, M., Stephen, M. T. COMPASS II: extended coverage for polymer and drug-like molecule databases. *J. Mol. Model.* **22**, 47 (2016)
- 56 Marrink, S. J., Risselada, H. J., Yefimov, S., Tieleman, D. P., de Vries, A. H. The

MARTINI Force Field: Coarse Grained Model for Biomolecular Simulations. *J. Phys. Chem. B* **111**, 7812-7824 (2007)

57 Van Der Spoel, D., Lindahl, E., Hess, B., Groenhof, G., Mark, A. E., Berendsen, H. J. C. GROMACS: Fast, Flexible, and Free. *J. Comput. Chem.* **26**, 1701-1718 (2005)

Acknowledgements

This work was supported by National Research Foundation of Korea (NRF) grants funded by the Korean Government (MSIP) (2020R1A2C3005939). Computational resources were from KISTI-HPC (KSC-2018-CHA-0005)

Author contributions

J.H.R designed the work. J.H.R. and S.K. directed the experiments. S.K. synthesized and characterized the compounds, studied the polymerization induced self-assembly behaviors, performed cell viability, confocal experiments for mitochondrial accumulation and mitochondrial dysfunction. B.J. performed flow cytometric analysis and western blot, managed in vivo experiment. S.S.K., E.M.G. and J.E.L. studied molecular simulations. S.J. performed cell TEM experiment. Y.S. performed SEM experiment. S.S. and D.K. contributed to synthesis of the compounds. C.K. contributed to the scientific discussion. The manuscript was written by S.K. and J.H.R. with the contribution from E.M.G., S.K.K. (Simulation part); B.J. (In-vivo part) ‡These authors contributed equally.

Additional Information

Competing financial interest.

The authors declare no competing financial interests.

Figures

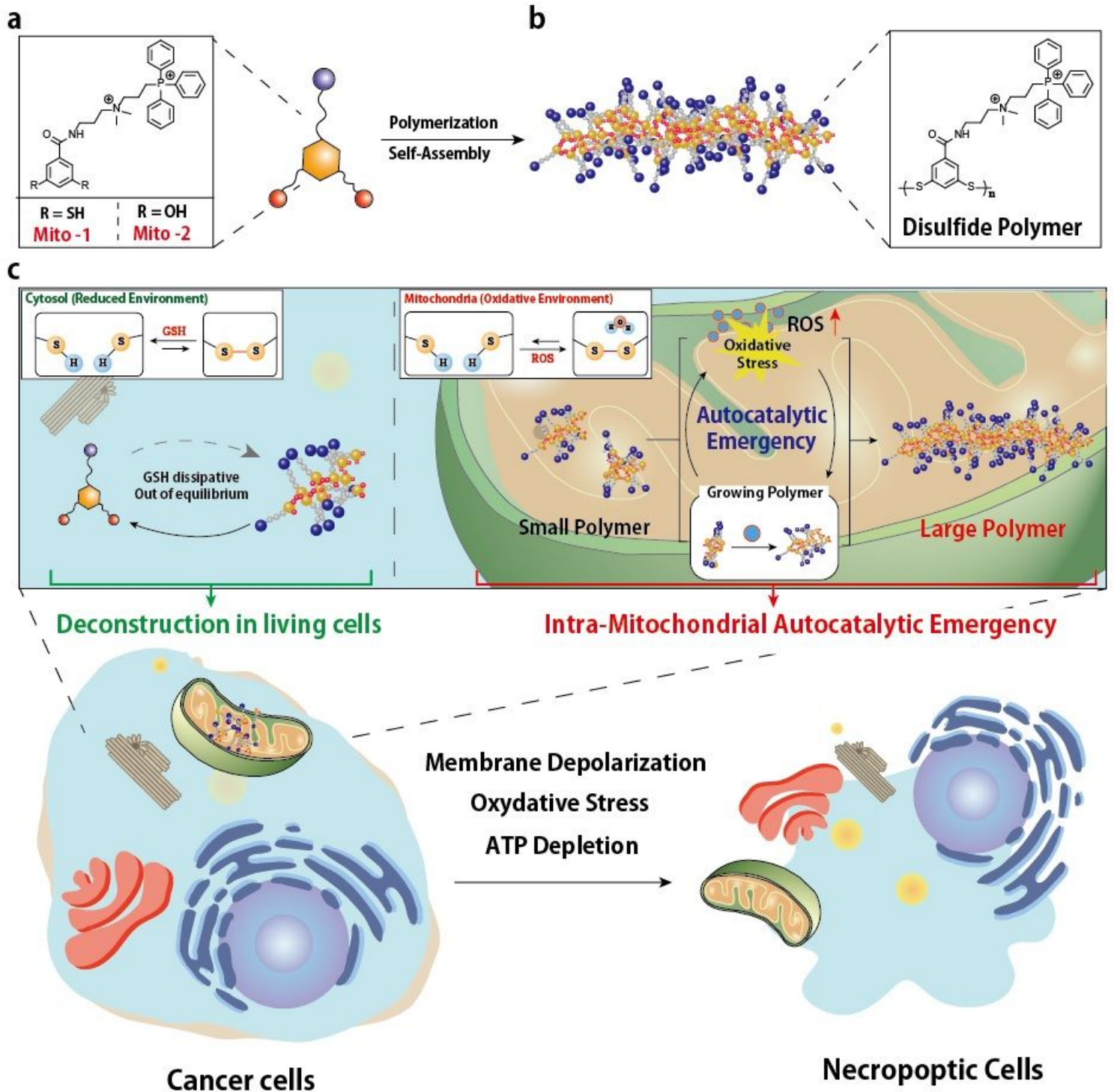


Figure 1

Intramitochondrial polymerization-induced self-assembly (Mito-PISA). Schematic illustration of Mito-PISA for controlling cancer cell necroptosis. a, Chemical structure of the monomer and b, polymerization-induced assembly by a disulfide polymer. c, Intramitochondrial polymerization can induce necroptosis and lead to mitochondrial dysfunction in cancer cells. Generally, the formation of disulfide bonds is

prohibited by the intracellular reductive environment. However, intramitochondrial accumulation of monomers facilitates polymerization, resulting in oxidative stress and generation of ROS. Increased levels of ROS provide effective conditions for the formation of large polymers, leading to mitochondrial dysfunction and activation of the necroptosis signaling pathway.

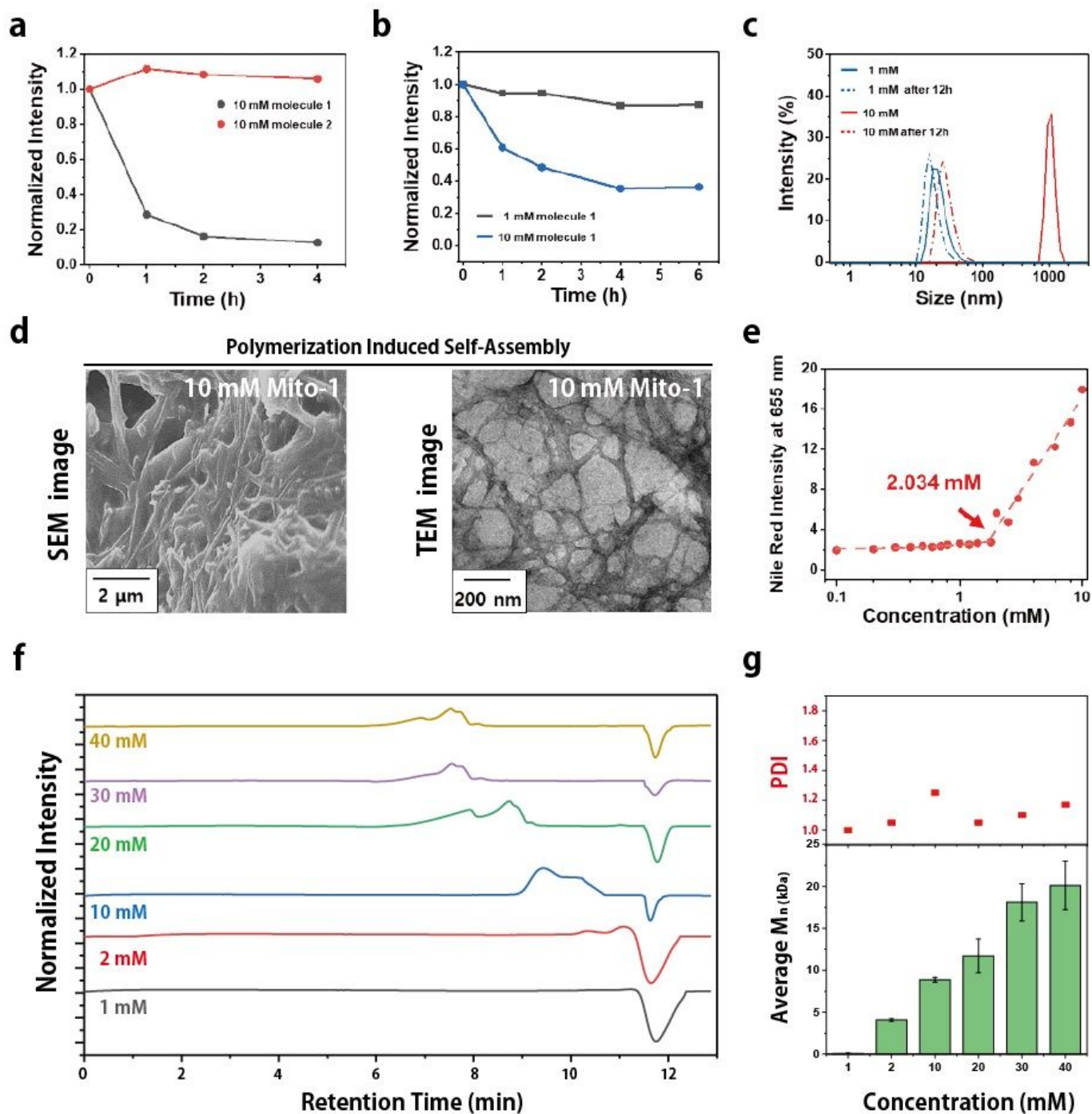


Figure 2

Polymerization using disulfide bond and self-assembly. a, Time-dependent intensity of the HPLC peaks attributed to Mito-1 and Mito-2 (10 mM) in a pH 8.0 buffer solution during polymerization for 4 h. The

amounts of Mito-1 and Mito-2 were quantified by HPLC and displayed as normalized intensity using the initial intensity. b, Time-dependent intensity of the HPLC peaks corresponding to Mito-1 (1 mM and 10 mM) in a mitochondrial mimic solution (pH 8.0, PBS buffer containing 10 mM GSH) during polymerization for 6 h. The amount of the monomer was quantified by HPLC and displayed as normalized intensity using initial intensity. c, Polymerization leads to self-assembly, which results in the formation of a nanostructure. Size distribution of Mito-1 (1 and 10 mM) in the mitochondrial mimic solution (pH 8.0, PBS buffer containing 10 mM GSH) at 0 and 12 h. The size of the polymeric structure was analyzed by DLS. d, SEM and TEM images of Mito-1 (1 and 10 mM) after stirring in the PBS buffer (pH 8) containing 10 mM GSH for 24 h. e, Critical aggregation concentration determination of Mito-1 in the PBS buffer (pH 8) containing 10 mM GSH. Steady fluorescence excitation spectra of Nile red at 645 nm and calibration plot obtained based on the emission spectra. f, GPC data for the polymerization of Mito-1 in the PBS buffer (pH 8) containing 10 mM GSH at various concentrations of the monomer (1, 2, 10, 20, 30, and 40 mM). g, Quantification of the average molecular weight and PDI values.

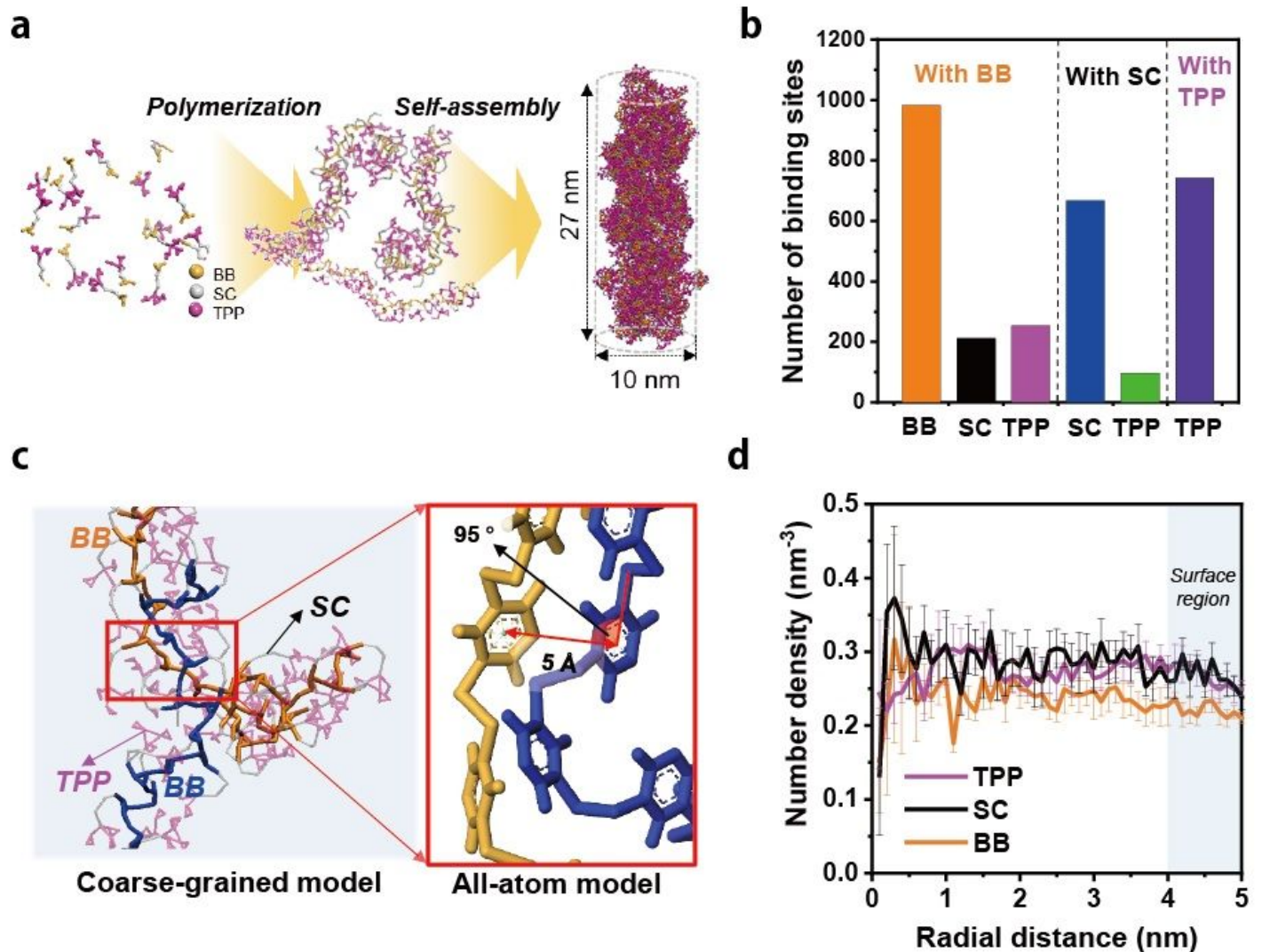


Figure 3

Simulation for the fibrous structure. a, Scheme showing polymerization and self-assembly of Mito-1 as well as the self-assembled fibrous structure obtained from the CGMD results. b, Number of binding sites between the BB, SC, and TPP groups in the fibrous structure. c, Binding states of two polymer chains at the surface of the fibrous structure. Stacking of the BB groups is shown in the red box. The distance and angle of the stacking interaction are also indicated. d, Number density of TPP, SC, and BB in the fibrous polymeric structure between the principal axis of the cylindrical shape to its surface. Surface region in the fibrous structure is indicated in light blue.

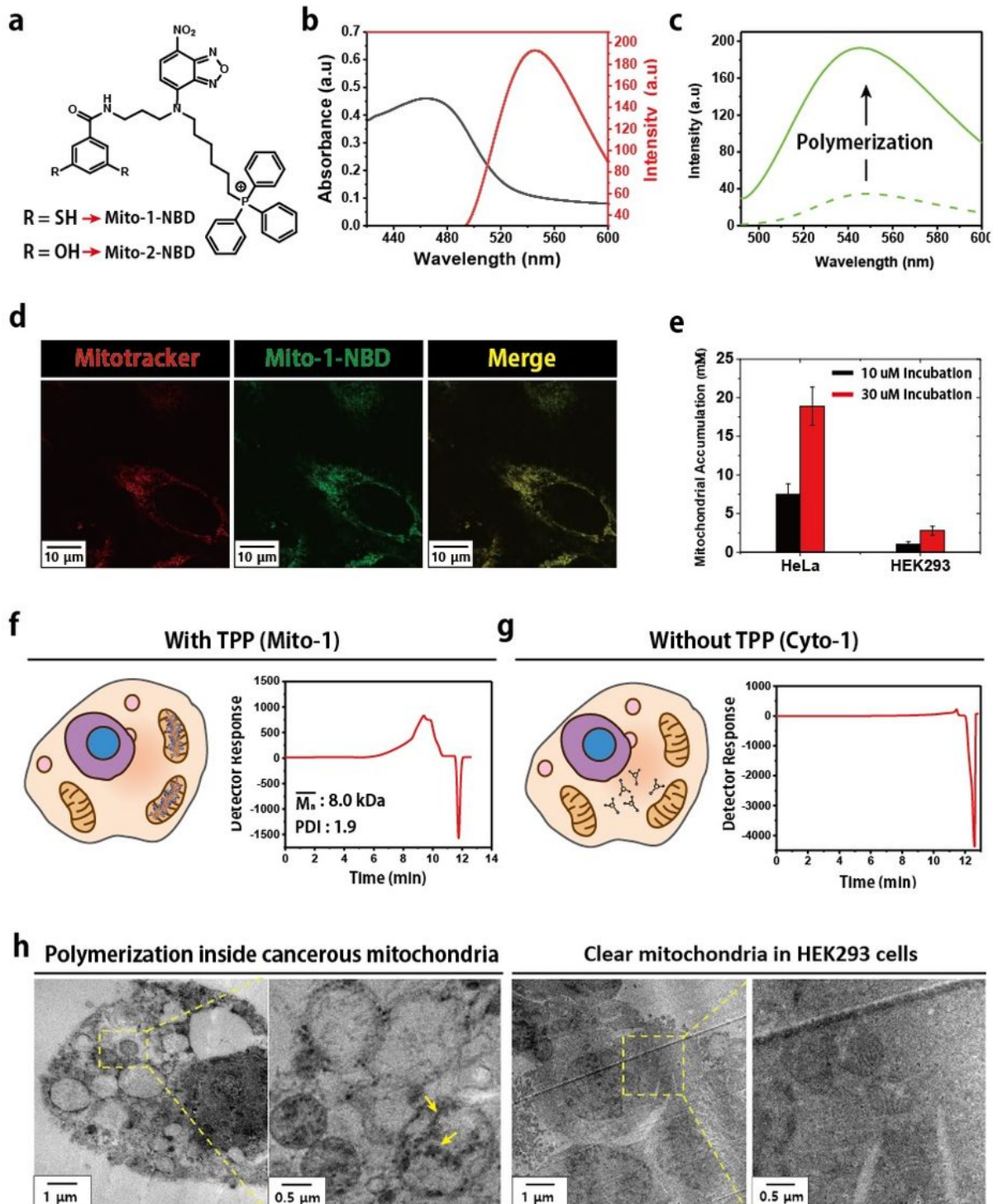


Figure 4

Intramitochondrial polymerization a, Chemical structures of Mito-1–NBD and Mito-2–NBD, derivatives of Mito-1 and Mito-2, respectively. b, Absorption and emission spectra of Mito-1–NBD. c, Emission spectra of 100 μM Mito-1–NBD (dashed line) and the polymerized product following stirring in the PBS buffer (pH 8) for 24 h (solid line). d, CLSM images showing the localization of Mito-1–NBD in the mitochondria of HeLa cells. The mitochondria were stained with MitoTracker Deep Red. e, Intramitochondrial accumulation of Mito-1–NBD in the HeLa and HEK293 cells treated with the conjugate for 4 h. The cells were washed and the mitochondria were isolated. The concentration of Mito-1–NBD was quantified by fluorescence measurements. f and g, GPC traces of intramitochondrial polymerization in the HeLa cells after 12 h of incubation with 30 μM Mito-1 and 30 μM Cyto-1, respectively. The cells were washed and lysed, and the polymers were characterized by GPC. h, TEM images of the HeLa and HEK293 cells treated with 30 μM Mito-1.

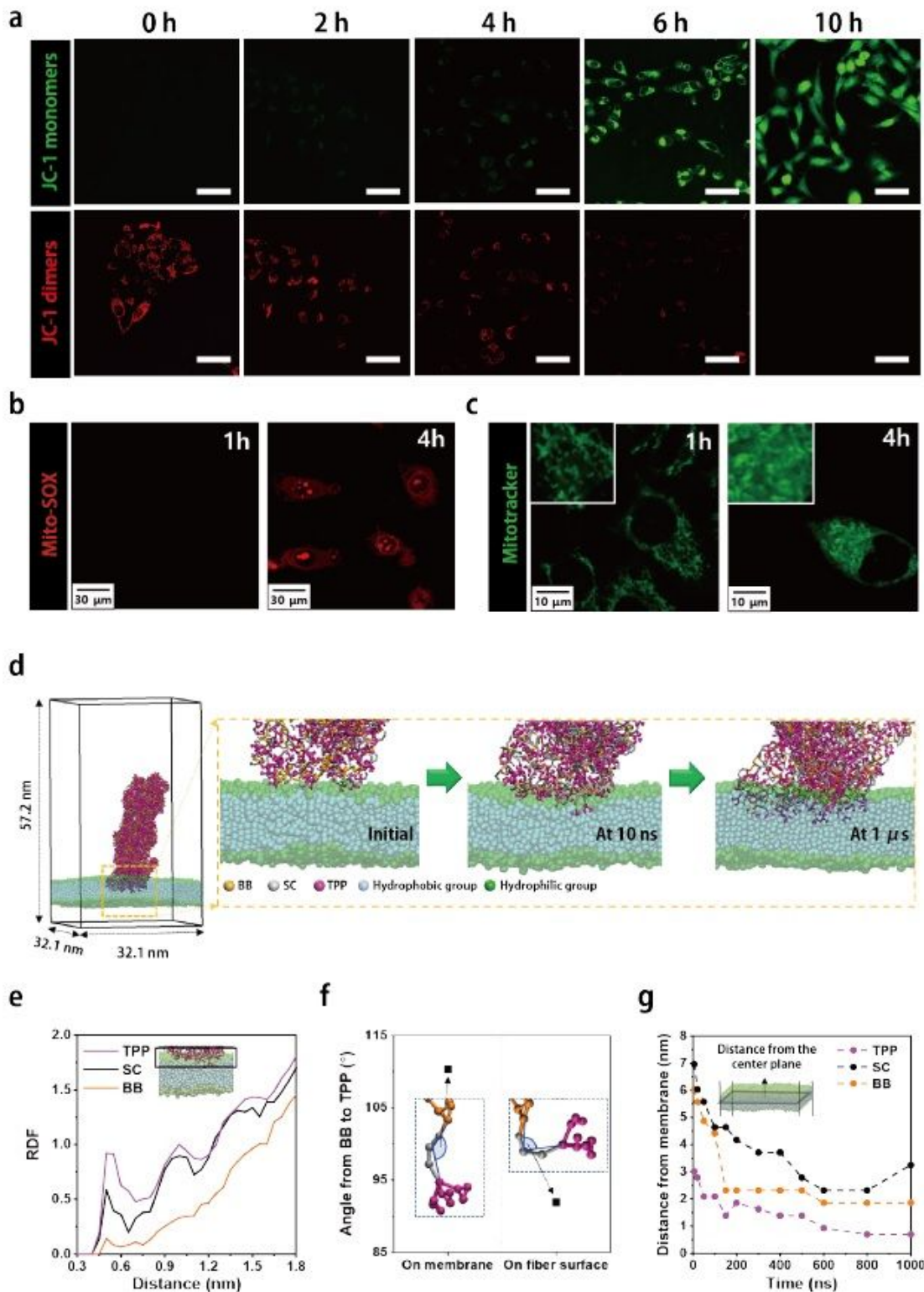


Figure 5

Intramitochondrial PISA induces mitochondrial dysfunction. a, Membrane depolarization of mitochondria was measured using the JC-1 dye. JC-1-labeled cells were observed by CLSM following treatment with 40 μ M Mito-1 for 10 h. The scale bar is 100 μ m. b, Confocal analysis showing the generation of ROS using MitoSOX. The HeLa cells were labeled by Mito-SOX after treatment with 40 μ M Mito-1 for 4 h. The intramitochondrial superoxide levels were measured by CLSM. c, Confocal microscopy image

showing mitochondrial fragmentation following intramitochondrial polymerization. The HeLa cells were incubated with 40 μM Mito-1 for 4 h and the mitochondrial condition was evaluated using MitoTracker green. d, The penetration of the fibrous structure into the cancer cell membrane and the penetrated states over the simulation time are shown in the yellow dotted box. Water molecules are omitted for clarity. e, Radial distribution function (RDF) of the BB, SC, and TPP moieties as well as of the hydrophilic groups of the lipids in the cell membrane at the initial stage of the penetration. The analyzed region is marked by a black box. f, Angles between BB and TPP in the fibrous structure on the cell membrane and on the surface of the fibrous structure. Blue dotted insets show the angles measured between the BB, SC, and TPP groups. g Distances of the BB, SC, and TPP moieties from the center of the cell membrane during the simulation.

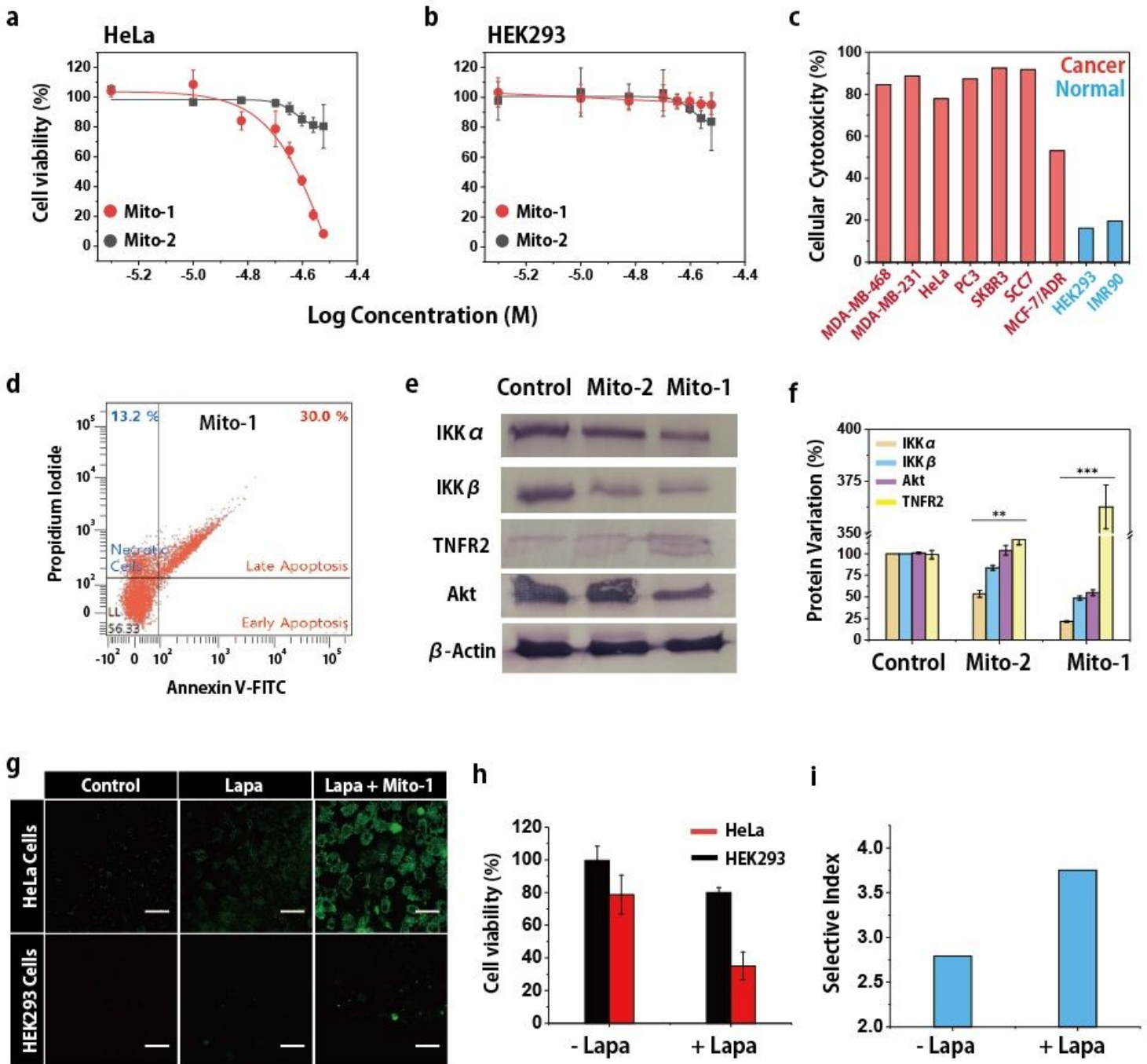


Figure 6

Intramitochondrial polymerization for cancer therapy. a, HeLa cells and b, HEK293 cells were treated with Mito-1 and Mito-2 for 24 h and the cellular viability was measured by an MTT assay. c, IC₅₀ values of Mito-1. Cellular toxicity toward MDA-MB-468, MDA-MB-231, HeLa, PC3, SKBR3, MCF7/ADR, HEK293, and IMR90 cell lines was analyzed. d, Flow cytometry analysis showing mitochondria associated necrosis induced by Mito-1. e, Western blot analysis of necroptotic proteins in HeLa cells treated with Mito-1 and Mito-2 for 12 h. The concentration of Mito-1 and Mito-2 was 40 μ M. f, Quantification of protein

variation based on western blot analysis. g, Fluorescence image showing intracellular ROS in HeLa and HEK293 cells treated with β -lapachone (Lapa) and Lapa + Mito-1. The levels of intracellular ROS were measured using the DCFH-DA assay after 4 h of Mito-1 exposure. h, Cytotoxicity of Mito-1 (20 μ M) toward HeLa and HEK293 cells treated with 5 μ M Lapa. The analysis showed synergistic effects of the treatment. i, Diagram indicating the selectivity index (IC50 of normal cells / IC50 of cancer cells) of synergistic therapy.

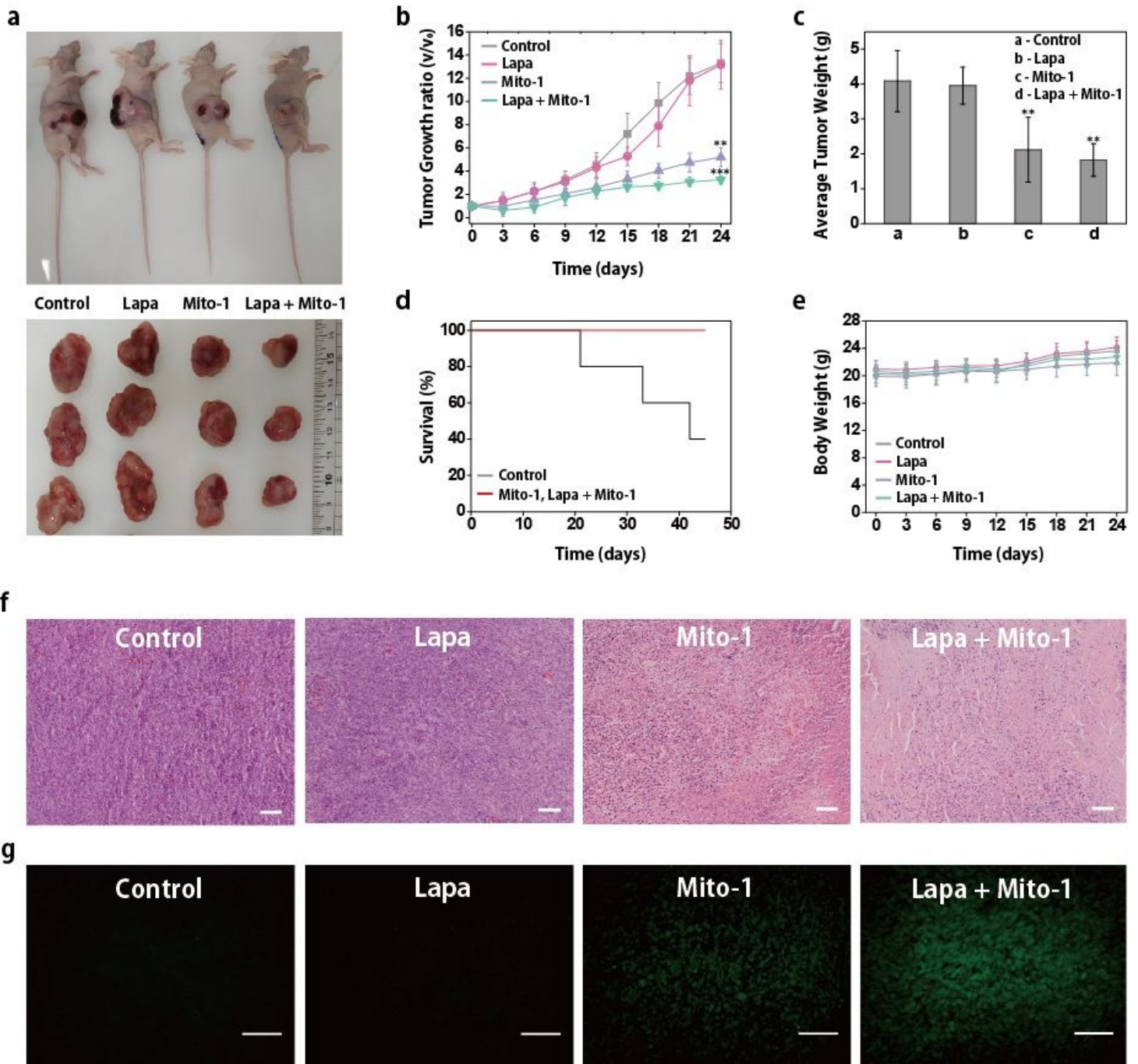


Figure 7

Anticancer efficacy of intramitochondrial polymerization. a, Images of mice and tumors after 24 days of treatment (n=6 per group). The dose of the Mito-1 and Lapa injections was 5 mg kg⁻¹. b, Observation of the tumor inhibitory effects in the control, Lapa, Mito-1, and Lapa+Mito-1 treatment groups. c, Weight analysis of the tumors collected after treatment for 24 days. d, Cumulative survival of different treatment groups exhibiting SCC7 tumors. All mice receiving Mito-1 and Lapa+Mito-1 treatment survived for 45 days. e, Weight change of 21 the mice in the tumor model after 24 days of treatment (n = 10 per group) The dose of the Mito- 1 and Lapa injections was 5 mg kg⁻¹. f, Hematoxylin and eosin staining and g, TUNEL assay of tumor sections treated with control, Lapa, Mito-1, and Lapa+Mito-1 for 24 days. The experiments were repeated three times and representative images are shown in the figure. Scale bar is 100 μm.

Supplementary Files

This is a list of supplementary files associated with this preprint. Click to download.

- [SliPISA.pdf](#)